ESA Ocean Colour Climate Change Initiative+ – Phase 2

System Vicarious Calibration of MERIS, MODIS, OLCI and VIIRS sensors processed by POLYMER

Ref: <Deliverable/v1.0>
Date: 20/04/2026

Contributors:	Name	Organisation	Role / Title
Lead Author(s)	Constant Mazeran	SOLVO	Lead of SVC method, gain computation, reporting
Contributing Author(s)	François Steinmetz	HYGEOS	Developer of POLYMER code
	Andrei Chuprin	PML	Satellite data extraction, match-up database
	Salem Salem	PML	Scientific review
Reviewer(s)	Elin Meek	PML	Project Manager
	Steve Groom	PML	Review
Final review and approval	Sarah Connors	ESA	Technical Officer

Digitally signed by Sarah Connors
Date: 2026.05.06 11:38:54 +01'00'

Change records	Date	Version
V1.0	15/04/2026	Initial version for CCI+ phase 2 with POLYMER4.17
V1.5	20/04/2026	Comments addressed

Contents

1. Executive summary

System Vicarious Calibration (SVC) historically has been introduced in the processing of ocean colour missions to meet the stringent requirements in absolute accuracy and across-sensor consistency of retrieved marine reflectance at bottom of atmosphere (BOA), so far unachievable by instrumental calibration alone. It consists of adjusting the top of atmosphere (TOA) radiometry by relying on high-quality field measurements concurrent with space acquisitions. In practice, vicarious gains are computed at each coincident point and each relevant wavelength to make the system comprising sensor and processing chain exactly match the in-situ marine reflectance.

Such an approach has been developed in the last year in the frame of the ESA Ocean-Colour Climate Change Initiative (OC-CCI), whose goal is to produce harmonised Climate Data Records based on several ocean colour sensors. OC-CCI has identified a non-standard atmospheric correction (AC), characterised by a non-linear inversion of the whole TOA spectrum, called POLYMER, which outperforms other ACs under climate change related criteria. Traditional SVC, where gains are calculated individually for each spectral band, cannot be applied because of the spectral coupling. Thus, a complete revisit of the SVC method has been necessary. The theoretical background developed in previous OC-CCI phases is currently applied without any fundamental change and is fully reminded in this ATBD for the sake of self-completeness. In short, the SVC problem is reformulated as a sensitivity problem between TOA and BOA radiometry. We demonstrate that it generally cannot be solved by the usual approach, and may even not have a strict solution, due to the spectral constraints of the marine model embedded in the AC. The SVC definition is extended in a least-square sense, and gains are computed by a generic numerical method that handles the spectral coupling. The method is a natural generalisation of the traditional SVC and reverts to it in case of a standard AC.

This approach is applied in the present OC-CCI+ Phase 2 to compute POLYMER gains for MERIS, MODIS, OLCI-A, OLCI-B VIIRSJ1 and VIIRSN sensors at the MOBY site (Marine Optical Buoy), characterised by oligotrophic waters and highly accurate measurements. While the POLYMER code (v4.17) and overall SVC method are identical to those used previous OC-CCI phases, new gains presented in this report relates to updates in both the satellite Level-1 archive (sometimes recalibrated by space agencies) and the in-situ data (extended match-up database and correction of bidirectional effects) and, marginally, the computations of gains at more individual bands actually not coupled in the POLYMER inversion (e.g. 709 nm for OLCI). Individual gains (i.e. for each match-up) show a remarkable stability in time for all considered bands and sensors, what allows the computation of mission-averaged gains, generally of small amplitude (less than 2%). Relevance of these gains is discussed, notably regarding their impact over other water types. A full validation is however out of scope of this ATBD. Finally, we summarise the fundamental specificities and limitations of SVC for POLYMER.

Introduction

Context and purpose of vicarious calibration

This work is carried out in the broad scope of remote sensing Essential Climate Variables (ECV) related to the biological state of the world's ocean, namely ocean colour radiometry (OCR), chlorophyll concentration and inherent bio-optical properties (WMO 2010; WMO 2022). Specifically, this study supports the Ocean Colour Climate Change Initiative (OC-CCI) of the European Space Agency (ESA) whose goal is to produce long-term time-series of ECVs based on several satellite-borne ocean colour sensors (Hollmann et al. 2013, Sathyendranath et al., 2019). While using multiple sources of remote-sensing data is the only feasible approach for building Climate Data Records (CDRs), it raises a critical question about the harmonisation of the various datasets (cf. Mélin et al. 2009, Maritorena et al. 2010, Brewin et al. 2014). Within the processing chain for generating the ECVs, OCR in the visible part of the spectrum is of utmost concern, since it is the primary ocean colour data and other ECVs, such as chlorophyll-a concentration, are derived quantities. Thus, very stringent requirements of 5% uncertainty in the blue and green channels and 0.5% stability over a decade have been defined for climate applications (WMO 2011, Zibordi et al. 2015); recently WMO (2022)[1] has clarified the metrological meaning of this uncertainty requirement, by specifying the coverage factor (*k*=2, i.e. two standard deviation for the confidence level).

OCR results from correction of the radiometry acquired by the sensor at top of atmosphere (TOA) and can be formally seen as the output of the system comprising sensor and processing chain. Hence the generation of a harmonised CDR requires i) a unique processing chain, which is mainly a matter of technical adaptation and ii) a consistent radiometric calibration between all space missions. System Vicarious Calibration (SVC) is the standard approach recommended by the Ocean Community to address the second requirement (Zibordi et al., 2025). Applied after the instrumental radiometric calibration (i.e. pre-launch as well as post-launch), it consists of adjusting the TOA radiometry through the use of ground-truth measurements, generally high-quality marine radiance, concurrent with space acquisitions. In practice, a vicarious calibration method produces gains at each validation point and each wavelength that make the {sensor + processing chain} system exactly match the field measurements. By construction, using the same reference in-situ measurements for different missions should harmonise the different CDRs, at least for marine and atmospheric conditions under which the processing chain performs similarly (see e.g. Mélin and Zibordi 2010 for a discussion on regional limitations).

The concept of vicarious calibration was introduced very early in ocean colour remote-sensing (e.g. Gordon 1987) to meet the specified accuracy of the water-leaving radiance, which forms only a small portion of the radiance measured at the sensor. To understand this aspect, let us first express the radiometry in term of reflectance (ρ), instead of radiance (L) primarily measured by the sensor, by using the following conversion:

$$\rho(\lambda) = \frac{\pi L(\lambda)}{F_0(\lambda)\cos\theta_s} \tag{1}$$

Where $F_0$is the extraterrestrial solar irradiance at time of acquisition and $\theta_s$the solar zenith angle.

Then the reflectance at sensor level ρ_{TOA}, at a given wavelength λ is classically modelled by:

$$\rho_t(\lambda) = t_g(\lambda) \cdot \left(\rho_R(\lambda) + \rho_a(\lambda) + \rho_{Ra}(\lambda) + t(\lambda)\rho_w(\lambda)\right) \tag{2}$$

Where t_g is the transmittance for gaseous absorption, ρ_R, $\rho_a$and $\rho_{Ra}$are respectively the reflectance for pure Rayleigh scattering, pure aerosol and multiple-scattering between air molecules and aerosols, ρ_w is the

[1] Note that therecent update of the WMO report in 2025 does not concern the Ocean Colour section.

desired marine reflectance and t the total upward and downward transmittance of the atmosphere. This formulation ignores implicitly diffuse reflection from whitecaps and sun glint contribution, which can be achieved by avoiding observations at high wind speed and the geometry of specular reflection

The contribution of the marine signal ρ_w to ρ_{TOA} is generally around 10% to 15%; over very clear waters the highest contributions occur in the blue wavelengths. Thus, the above-mentioned requirement of 5% accuracy for the water leaving reflectance translates into an accuracy of 0.5% for the TOA reflectance, which is already out of the scope of instrumental calibration for any mission (Eplee et al. 2011, Delwart and Bourg 2013). The atmospheric correction (AC) process, whose goal is to retrieve ρ_w from measurement of ρ_{TOA}, adds further uncertainty which can be substantial. Hence, vicarious calibration has been historically introduced to complete the imperfect instrumental radiometric calibration, compensate AC errors and reach a higher performance for the whole system.

This general consideration must, however, be clarified by considering the exact link between ρ_w and ρ_{TOA}. Atmospheric correction consists formally of inverting Eq. (2):

$$\rho_w(\lambda) = \frac{\frac{\rho_t(\lambda)}{t_g(\lambda)} - \left(\rho_R(\lambda) + \rho_a(\lambda) + \rho_{Ra}(\lambda)\right)}{t(\lambda)} \tag{3}$$

In standard atmospheric corrections (e.g. Gordon and Wang 1994, Antoine and Morel 1999), the unknown aerosol signal, involving atmospheric reflectance and transmittance is inferred from two near-infrared (NIR) bands only. Typically, the algorithm uses bands around 765 nm and 865 nm to compute aerosol optical thickness and identify one amongst a set of precomputed aerosol models. From a spectral point of view, this means that $\rho_w(\lambda)$ depends on the TOA radiometry at band λ itself in the visible and at two other bands in the NIR. If the NIR bands are well-calibrated, then the TOA relative error $\frac{\Delta\rho_t}{\rho_t}$ in the visible leads to a relative error at sea level of:

$$\frac{\Delta\rho_w}{\rho_w}(\lambda) = \frac{\Delta\rho_t}{\rho_t}(\lambda) \Big/ \frac{t_g t \rho_w(\lambda)}{\rho_t(\lambda)} \tag{4}$$

The denominator of (4) represents exactly the contribution of marine reflectance to TOA signal. This equation justifies the well-known rule previously stated: “If $t\rho_w$ is 10% of ρ_t, and we want ρ_w with an uncertainty of ±5%, one would expect that it would be necessary to know ρ_{TOA} with an uncertainty of no more than ±0.5%” (Gordon 1998). More recently the basic equation (4) has been exploited in detail by Zibordi et al. (2015) to derive specifications for the quality of in-situ data for the purpose of CDRs. However, it is important to emphasise that this overall algebra is intrinsically linked to the standard atmospheric correction scheme, in particular, to the decoupling between all bands in the visible as well as to the supposed perfect calibration of NIR bands. This is why the system of sensor and processing chain must be considered as a whole, and has led to the concept of system vicarious calibration (Gordon 1987, Evans and Gordon 1994). In particular, the first attempts for SeaWiFS tried to simultaneously calibrate both visible and NIR bands (Gordon 1998, Eplee et al. 2001). It is worth noting that Gordon (1998) concluded the previous rule with following statement, which is not important for standard atmospheric correction but very relevant in the present study: “However, as several bands are used in the atmospheric correction of a single band, the variation of the calibration error from band to band is also important”.

Reminder of the standard method

While several approaches have been tested since end of the 1980s, we will restate only the successful method of Franz et al. (2007) which has been operationally used by NASA for SeaWiFS and MODIS and now for PACE (Frouin et al., 2025), by ESA for MERIS with minor adaptation (Lerebourg et al. 2011), by NOAA for VIIRS (Wang et al., 2016) and by EUMETSAT for OLCI (Mazeran and Ruescas, 2020). As with any system vicarious calibration, it relies strongly on the atmospheric correction scheme (Gordon and Wang 1994, Patt et al. 2003) and in particular on two key aspects:

- A decoupling between NIR and visible bands: two bands in the NIR are used to detect the atmosphere (aerosol content), and the atmospheric correction is successively applied in the visible
- A decoupling between all visible bands: the correction is applied independently band per band

For historical reasons we will refer the class of atmospheric correction algorithms that fulfils these criteria to as *standard atmospheric correction*, in contrast to alternative approaches coupling all bands in the visible and in the NIR. Consequently, it enables an independent (successive) vicarious calibration of the NIR and visible bands, which we will also refer to as *standard*.

For any wavelength, in both regions of the spectrum, the method seeks to reconstruct the true (or targeted) TOA signal ρ_t^t using indirect measurements or assumptions. Comparison with actual sensor acquisition provides vicarious calibration gains:

$$g(\lambda) = \frac{\rho_t^t(\lambda)}{\rho_t(\lambda)} \tag{5}$$

In essence, vicarious calibration assumes that these gains, computed in ideal conditions, represent a systematic bias of the sensor and processing chain system.

The method is conducted in two steps. First, in the NIR, the targeted signal is computed over stable and homogenous oligotrophic waters (typicaly the South Pacific Gyre, SPG), where the marine signal can be neglected:

$$\rho_t^t(\lambda_{NIR}) = t_g(\lambda_{NIR})\big(\rho_R(\lambda_{NIR}) + \rho_a^t(\lambda_{NIR}) + \rho_{Ra}^t(\lambda_{NIR})\big) \tag{6}$$

The method assumes that the aerosol model is known (maritime atmosphere and relative humidity) and that the longest wavelength is already well calibrated (for example, NASA uses $g(865) = 1$ for SeaWiFS and $g(869) = 1$ for MODIS). It is then possible to predict the TOA signal at the shortest NIR wavelength and deduce a calibration factor. After this NIR calibration, all quantities derived by the atmospheric correction can be considered as reference: aerosol signal $\rho_a^t(\lambda) + \rho_{Ra}^t(\lambda)$ and diffuse transmittance $t^t(\lambda)$, at any wavelength λ.

Second, in the visible (VIS), the targeted signal is computed using reference in-situ marine reflectance $\rho_w^t(\lambda)$, acquired concurrently with the satellite measurement:

$$\rho_t^t(\lambda) = t_g(\lambda)\big(\rho_R(\lambda) + \rho_a^t(\lambda) + \rho_{Ra}^t(\lambda) + t^t(\lambda)\rho_w^t(\lambda)\big) \tag{7}$$

The criticality of these in-situ measurements, which calibrate ocean colour mission at global scale and on the long-term, requires rigorous protocols in the instrumentation. To date, the Marine Optical Buoy (MOBY; Clark et al. 1997) located off the Lanai Hawaiian island has constituted the reference site for deriving consistent SVC gains since 1997, due to its oligotrophic waters and highly accurate measurements (Clark et al. 2003). On top of that, SVC needs stringent protocols to build match-up with satellite data (Mueller et al. 2003; Bailey and Werdell 2006).

We insist on the fact that the targeted signal in Eq. (7) is constructed with very same elements as that of the atmospheric correction, cf. Eq. (3), in particular radiative transfer look-up tables, so that there is a perfect consistency between atmospheric correction and calibration. By construction, the system vicarious calibration in the visible will make the algorithm exactly match the in-situ signal, whatever the real source of error in the system (from sensor or algorithm or probably from both).

Technically, vicarious gains given in Eq. (5) are first computed pixel by pixel for each match-up. The perfect match with in-situ data demonstrates the relevance of these so-called individual gains. The pixel-per-pixel gains are then spatially averaged, providing a unique gain per match-up, for each wavelength. Eventually, matchup-per-matchup gains are temporally averaged, yielding a unique set of gains $\bar{g}(\lambda)$ at each wavelength, over the entire mission lifetime. To minimise impact of outliers, Franz et al. (2007) used the mean of the semi-interquartile range (MSIQR, mean of data within the 25th and 75th percentiles) for both spatial and temporal averaging:

$$\bar{g}(\lambda) = \underset{time}{\mathrm{MSIQR}}\left(\underset{space}{\mathrm{MSIQR}}\big(g(\lambda)\big)\right) \tag{8}$$

Because of the variability in marine reflectance errors, the mean gains $\bar{g}$ in the visible can only remove biases, i.e. average systematic errors. Hence the reference dataset must be representative of most common atmospheric and marine conditions.

We emphasize that all recent works on SVC remain within this framework of aerosol detection in the NIR only (Zibordi et al., 2025), and do not introduce new methodological foundation that could be relevant for POLYMER (next section). For instance, Wang and Liang (2025) have extended the method of Franz et al. (2007) for SWIR-based AC, using the two-step approach and very same assumptions (aerosol detection in the NIR-SWIR where marine signal is negligible). Another example from Wang et al. (2025) concerns the SVC of the Ultraviolet Imager (UVI), a sensor onboard the Chinese HY-1C platform not endowed with NIR bands; here the solution consisted in using the concurrent NIR measurements of the COCTS sensor also onboard HY-1C to detect aerosols, and then in applying the standard SVC approach from NIR to UV. Adaptation may also concern the unavailability of in-situ data. A noticeable case is the SVC of GOCI, a geostationary sensor focused on the North-East Asian region, hence, without any match-ups over SPG and MOBY: in the NIR, authors have considered a mix of aerosol models more representative of the local atmosphere (50% and 99% relative humidity), and in the VIS they have used less accurate in-situ data, generally considered for validation (measurements from ASD-FieldSpec and TriOS-RAMSES radiometers). More recently, the need to quickly compute SVC gains for PACE in its early phase was achieved by complementing the usual MOBY instrument with radiometers installed on an autonomous profiling float (HyperNav, Barnard et al. 2024), providing a large number of match-ups over other regions in the world (Chamberlain et al. 2024; Frouin et al., 2025). In Europe, the key on-going activity about SVC is precisely about the design of a dedicated long-term infrastructure, as part of the Copernicus program (EUMETSAT, 2017). Candidate technologies and sites in European waters have been investigated (Zibordi and Mélin 2017; Antoine et al., 2020; Liberti et al., 2020), targeting clear waters and low aerosol load, which are the baseline assumptions for standard AC and standard SVC.

Challenges of SVC for non-standard atmospheric correction

In the last decade there has been an emergence of alternative ocean colour algorithms which do not use the NIR to identify aerosol and may even not follow the standard formulation (Eq. (3)). These atmospheric corrections makes use of most of the available radiometry from blue to NIR-SWIR channels, with the objective of better addressing optically complex waters with significant scattering in the NIR (IOCCG, 2025), of being more robust to radiometric noise, of having a larger spectral basis for better aerosol propagation or of inverting more complex physical effects such as thin clouds, sun glint residual and absorbing aerosols. Without being comprehensive, most of these techniques are referred to as artificial neural networks (e.g. Doerffer and Schiller 2007, Schroeder et al. 2007, Fan et al. 2021), spectral matching algorithms (e.g. Chomko et al. 2003, Spurr et al. 2007, Kuchinke et al. 2009, Steinmetz et al. 2011) or Bayesian approach (e.g. Frouin and Pelletier 2015). Within the OC-CCI project, POLYMER (Steinmetz et al. 2011) was successfully tested in a first phase on the MERIS sensor (Müller et al. 2015) and is being used for harmonisation of all sensors (except SeaWiFS). It is described in more detail in the next section and will serve as a practical case to illustrate more generally our findings about SVC for non-standard AC. Note than an evolution of POLYMER was investigated more recently as part of the EUMETSAT SACSO study (Steinmetz and Mazeran, 2021), relying on the same spectral matching approach but involving an alternative aerosol model and numerical optimization scheme; since this variant is not considered in current OC-CCI phase, it is not further detailed, while overall theoretical findings presented in this report remain applicable.

A common feature of all non-standard ACs is to determine either explicitly or implicitly the atmospheric path signal from knowledge of several bands in the visible, and possibly the NIR bands, and requires embedding a marine model in the algorithm. This is opposed to the standard approach, which is based on the black pixel assumption in the NIR, and does not, at least for clear waters, impose any modelling hypothesis on the marine reflectance (Gordon 1978, Siegel et al. 2000). From a purely radiometric point of view, the retrieval of marine reflectance at band λ_i by any atmospheric correction scheme can be formally written by:

$$\rho_{wN}(\lambda_i) = f_i\big(\rho_t(\lambda_1), \cdots, \rho_t(\lambda_n)\big), \;\; i = 1 \dots m \tag{9}$$

where the m functions f_i express the link to TOA radiometry and may also depend on other non-radiometric parameters such as ancillary data, geometrical conditions, physical constants, etc., not made explicit in the present context. These functions may be more or less complex depending on the atmospheric correction scheme, and may even not be explicit, such as in artificial neural networks. In Eq. (9) we note n the number of TOA bands used as input to the atmospheric correction and m the number of bottom of atmosphere (BOA) bands at which a marine reflectance is provided, with $m \leq n$. Note also that for convenience we deal with fully normalised marine reflectance ρ_{wN} (see Morel and Gentili 1996 for Case-1 waters), that is, we include the bidirectional reflectance distribution function (BRDF) correction in functions f_i for a direct comparison with in-situ measurements in normalised condition.

Such algorithms make the standard SVC approach inoperative for two reasons. The first technical reason is that Eq. (9) is not algebraically invertible (assuming that it would even be invertible), making it impossible to reconstruct the targeted TOA signal ρ_t^t from knowledge of the target marine signal ρ_{wN}^t. Hence the definition of vicarious calibration gains Eqs. (5)-(7) simply cannot be applied. The second reason is that the SVC approach relies intrinsically on the linear response of the marine reflectance in one band with respect to the TOA signal at this very same band (see Eq. (3)). This decoupling and linearity are no longer true with non-standard atmospheric corrections, so that changing (calibrating) the radiometry at one band also impacts the marine reflectance at other bands. This effect is illustrated in *Figure 1* for a typical MODIS TOA spectrum over clear water, processed on the one hand by the SeaDAS standard algorithm (Baith et al 2001) and on the other hand by POLYMER (Steinmetz et al. 2011, see detailed description in section 2). In both cases the remote-sensing marine signal, prior to any SVC, is too high when compared to the in-situ measurement at all bands and especially by around 25% at 412 nm. A calibration gain of -1% is then applied on $\rho_t(412)$ and results into:

- A relative change of about -7% on $\rho_w(412)$ only, in case of SeaDAS
- A relative change of less than -2% on ρ_w at 412 nm, becoming positive and growing with wavelength, from about +3% at 443 nm to +30% at 667 nm, in case of POLYMER

This example shows that it may be possible to make the POLYMER $\rho_w(412)$ match the in-situ measurement by decreasing $\rho_t(412)$, but with a much greater amplitude than for SeaDAS. More importantly, this change causes biases in other bands and calibrating the TOA signal at other bands also impacts $\rho_w(412)$. Hence the vicarious gain at 412 nm cannot be computed independently.

SeaDAS POLYMER

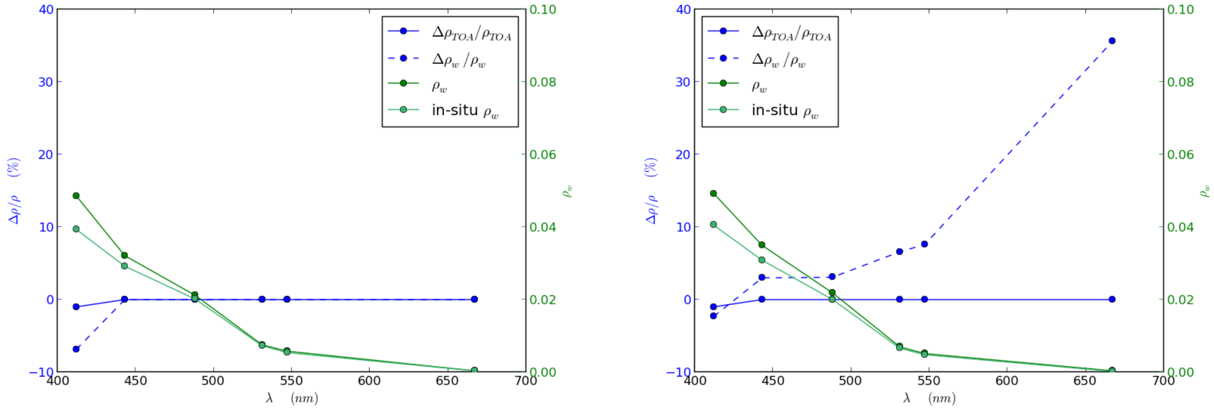

Figure 1. Relative change of the marine reflectance (dashed blue) due to a TOA relative change of 1% at 412 nm (solid blue, left Y-axis), for SeaDAS algorithm (left) and POLYMER (right) over a typical clear water spectrum. Clear and dark green lines represent respectively the in situ and satellite marine reflectance (right Y-axis)

In conclusion, vicarious gains for non-standard atmospheric correction are all spectrally coupled. At this stage, a relevant object to inspect the spectral coupling of the SVC problem is the Jacobian matrix of the generic function f defining the atmospheric correction in Eq. (9):

$$\nabla f = \begin{pmatrix} \frac{\partial f_1}{\partial x_1} & \cdots & \frac{\partial f_1}{\partial x_n} \\ \vdots & \ddots & \vdots \\ \frac{\partial f_m}{\partial x_1} & \cdots & \frac{\partial f_m}{\partial x_n} \end{pmatrix} \tag{10}$$

This matrix expresses the sensitivity of the BOA quantity (marine reflectance) on the TOA radiometry; its coefficients can be written more explicitly by $\partial f_i/\partial x_j = \partial\rho_{wN}(\lambda_i)/\partial\rho_t(\lambda_j)$. An example of such matrix is given on *Figure 2*, for a typical clear water pixel and at six wavelengths in the visible ($m = n = 6$). Note that its computation requires numerical differentiation, as will be described in section 2. The colour of each cell represents the absolute value of the partial derivative, while the sign is written in the cell. In the SeaDAS example (left image), the NIR iteration scheme (Bailey et al. 2010) has been de-activated, which yields a diagonal matrix, and reflects the decoupling of the standard atmospheric correction. Looking into details actually shows a slight extra-diagonal dependence in $\rho_t(443)$ and $\rho_t(547)$, due to the bidirectional effect correction, using these two bands in the chlorophyll estimate (Morel and Gentili 1996); this sensitivity is, however, extremely small compared to the diagonal terms. The right image displays the Jacobian matrix over same condition for POLYMER and shows a totally different structure. First the matrix is no longer diagonal, characteristic of the spectral coupling. Then for a given row (i.e. given $\partial\rho_{wN}(\lambda_i)$), diagonal terms are sometimes smaller than extra-diagonal terms. This means that the spectral constraints of the atmospheric correction are stronger than the TOA radiometry itself. For instance, $\rho_{wN}(412)$ is much more sensitive to $\rho_t(488)$ and $\rho_t(531)$ than to $\rho_t(412)$ itself. Also relative change between bands may be of opposite sign: for instance a positive change at $\rho_t(443)$ increases $\rho_{wN}(531)$ but a positive change at $\rho_t(531)$ decreases $\rho_{wN}(443)$. Eventually, bands near the red, such as 547 and 667nm, are weakly sensitive to the TOA radiometry (rows $\partial\rho_{wN}(547)$ and $\partial\rho_{wN}(667)$), but inversely they impact marine reflectance in the blue (columns $\partial\rho_t(547)$ and $\partial\rho_t(667)$), so are part of the SVC problem.

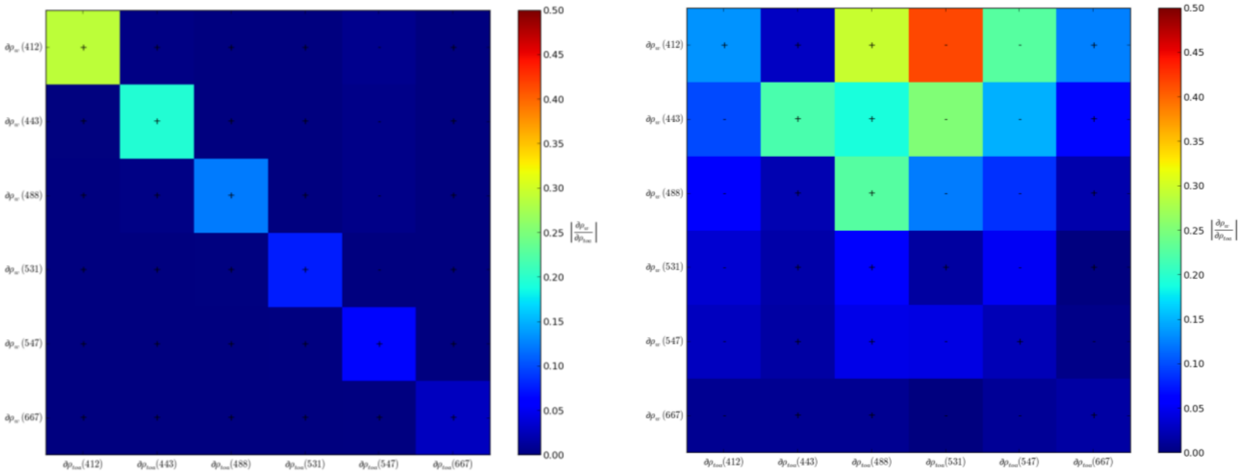

Figure 2. Jacobian matrix on a typical clear water pixel for SeaDAS (left) and POLYMER (right).

Hence, the structure of the Jacobian matrix illustrates the complexity of the vicarious calibration problem, which is now described as a problem of BOA sensitivity to the TOA radiometry. In this respect the behaviour of algorithms such as POLYMER is significantly different compared to standard atmospheric corrections. It requires us to have a broader understanding of the SVC problem than we have been used to.

Generalizing the SVC definition

Since atmospheric correction schemes following the generic formalism of Eq. (9) preclude computing the gains with standard equations (5)-(7), we propose generalising the definition of gains. The intrinsic definition of a set of SVC gains $(g_1, g_2, \cdots, g_m)$ associated to wavelengths $\lambda_1, \lambda_2, \cdots \lambda_m$ is that it allows the exact retrieval of the targeted signal ρ_{wN}^t at the same bands; this can be written as

$$f_i\big(g_1 * \rho_t(\lambda_1), \cdots, g_m * \rho_t(\lambda_m), \rho_t(\lambda_{m+1}), \cdots, \rho_t(\lambda_n)\big) = \rho_{wN}^t(\lambda_i), \;\; i = 1 \dots m \qquad (11)$$

In its most generic form, Eq. (11) must be understood as a non-linear system of m equations and m unknowns, which defines implicitly the gains. It is important that the number of gains cannot be greater than the number of available information, m, so that $n - m$ bands cannot be vicariously calibrated. For the sake of simplicity, we have sorted the m calibrated channels in the lowest positions, without any assumption on the real order of the wavelengths.

We will refer to Eq. (11) as the *strict* SVC problem because a strict retrieval of the in-situ data is expected, in accordance with the standard SVC definition. This definition however does not ensure existence and uniqueness of a solution, which is the general impediment of any non-linear system, depending on the non-linearity of the atmospheric correction (i.e. of functions f_i). We will demonstrate in section 3 that the strict SVC problem applied to POLYMER allows solution only under very particular conditions, and furthermore that there is a multiplicity of possible gains. The only way to deal with such cases is to solve Eq. (11) in a weaker sense, i.e. in a least-square sense. For such purpose we will define the *optimal* SVC problem as finding a set of l gains $g = (g_1, g_2, \cdots, g_l)$ with $l \leq m \leq n$ which minimises the discrepancy between the retrieved and targeted marine signal, for a given χ^2 cost function:

$$\chi_{SVC}^2(g) = \sum_{i=1}^{m} \Big(\rho_{wN}^t(\lambda_i) - f_i\big(g_1 * \rho_t(\lambda_1), \cdots, g_l * \rho_t(\lambda_l), \rho_t(\lambda_{l+1}), \cdots, \rho_t(\lambda_n)\big)\Big)^2 \qquad (12)$$

This minimisation problem also provides an implicit definition of the gains, but now ensures existence of at least one solution to the SVC. Furthermore, if by chance the strict SVC admits a solution, then it will also be a solution of the optimal SVC. Hence this latter formalism will be considered by default in the following. Note that the cost function χ_{SVC}^2 could be refined by weighting each square of the sum, typically by uncertainty at each band, without changing the aim of the method. This option is not retained in the present work, first because of lack of knowledge in the remote-sensing uncertainty and second because of spectrally white uncertainty of the MOBY data considered here (between 2 and 4% from 412 to 666nm, see Brown et al. 2007).

A noticeable difference between the strict (Eq. (11)) and optimal (Eq. (12)) SVC is the number of bands to be calibrated. The strict SVC needs as many TOA gains as marine reflectance bands, i.e. m. On the contrary the optimal SVC can relax the number of gains to $l \leq m$, although all m information at BOA are kept in the cost function. For example, we may search gains at two bands (λ_1, λ_2) to best match in-situ data of four bands $(\lambda_1, \lambda_2, \lambda_3, \lambda_4)$, keeping in mind that the TOA radiometry at the two first bands impacts all fours bands at BOA. This flexibility will be used to solve the issue of non-uniqueness.

Finally let us emphasise that this revisited definition of SVC in Eq. (12) is a natural extension of the standard SVC formalism (Eqs. (5)-(7)), in the sense that it leads to the same gains when applied to the standard atmospheric correction scheme. This can be verified by fitting the standard scheme Eq. (3) in our general formalism with

$$f_i(\rho_t(\lambda_1), \cdots) = C_{BRDF}(\lambda_i) \frac{\frac{\rho_t(\lambda_i)}{t_g(\lambda_i)} - \left(\rho_R(\lambda_i) + \rho_a(\lambda_i) + \rho_{Ra}(\lambda_i)\right)}{t(\lambda_i)}, \ i = 1 \ldots m \tag{13}$$

Where $C_{BRDF}(\lambda_i)$ is the BRDF correction factor converting marine reflectance from sensor geometry (ρ_w) to normalised geometry (ρ_{wN}). This factor generally depends on the bio-optical content just beneath the sea surface, which in operation can only be deduced from the radiometry and induces a spectral coupling in the ρ_{wN}. In the context of vicarious calibration, this knowledge is provided by the in-situ data, breaking the dependence of C_{BRDF} on the sensor radiometry. Remember also that atmospheric quantities do not depend on radiometry of bands $1 \ldots m$, because aerosol detection is conducted at other bands in the NIR. Thus f_i are simple linear functions of $\rho_{TOA}(\lambda_i)$ only and the optimal SVC problem, computable through $\nabla \chi^2_{SVC} = 0$, simplifies immediately to the strict SVC problem, written as a linear system:

$$J \begin{pmatrix} \rho_t(\lambda_1) & \cdots & 0 \\ \vdots & \ddots & \vdots \\ 0 & \ldots & \rho_t(\lambda_m) \end{pmatrix} \begin{pmatrix} g_1 \\ \vdots \\ g_m \end{pmatrix} - \begin{pmatrix} \tilde{\rho}_{path}(\lambda_1) \\ \vdots \\ \tilde{\rho}_{path}(\lambda_m) \end{pmatrix} = \begin{pmatrix} \rho^t_{wN}(\lambda_1) \\ \vdots \\ \rho^t_{wN}(\lambda_m) \end{pmatrix} \tag{14}$$

Where $\tilde{\rho}_{path}(\lambda_i) = C_{BRDF}(\lambda_i)\left(\rho_R(\lambda_i) + \rho_a(\lambda_i) + \rho_{Ra}(\lambda_i)\right) / \ t(\lambda_i)$ and the Jacobian matrix J of the atmospheric correction is diagonal:

$$J = \begin{pmatrix} \frac{C_{BRDF}(\lambda_1)}{t_g(\lambda_1)t(\lambda_1)} & \cdots & 0 \\ \vdots & \ddots & \vdots \\ 0 & \ldots & \frac{C_{BRDF}(\lambda_m)}{t_g(\lambda_m)t(\lambda_m)} \end{pmatrix} \tag{15}$$

The trivial solution is given by:

$$g_i = \frac{t_g(\lambda_i)\left(\rho_R(\lambda_i) + \rho_a(\lambda_i) + \rho_{Ra}(\lambda_i) + t(\lambda_i)\frac{\rho^t_{wN}(\lambda_i)}{C_{BRDF}(\lambda_i)}\right)}{\rho_t(\lambda_i)}, \ i = 1 \ldots m \tag{16}$$

We recognise identical gains as the standard definition in Eqs. (5)-(7), with $\frac{\rho^t_{wN}}{C_{BRDF}}$ being the targeted marine signal converted to sensor geometry.

This ATBD will show that such a new formalism is necessary and efficient to handle SVC for non-standard atmospheric corrections. Section 2 presents the material (POLYMER algorithm, in-situ data used for calibration and validation, satellite data) and introduces the OC-CCI numerical method to solve the optimal SVC. In section 3, a theoretical analysis of POLYMER atmospheric correction demonstrates the problem of non-uniqueness and non-existence of gains in the strict sense. We present detailed gains in section 4 as defined by the optimal SVC, for MERIS, MODIS, OLCI-A, OLCI-B, VIIRSJ1 and VIIRSN. In section 5, we analyse the meaning of these average gains, discuss their relevance and limits (notably by a quick assessment of their impact over different water types) and finally summarise the key conclusion of SVC for non-standard AC like POLYMER.

2. Data and method

POLYMER algorithm

POLYMER atmospheric correction was first introduced in Steinmetz et al. (2011) for the MERIS sensor and stands for "POLYnomial based algorithm applied to MERIS". Its initial motivation was to correct for the sun glint effect, which affects a large part of the MERIS swath. Authors showed a roughly equivalent performance of the inversion inside and outside the glint area, hence increasing the usual coverage of MERIS data. The algorithm has since been updated within the ESA OC-CCI project as described in Steinmetz et al. (2015). The main difference consists in using an alternate water reflectance model including bidirectional correction to sun at zenith and sensor at nadir, based on Park and Ruddick (2005) and more suited to case 2 waters than the previous model. Other updates relate to of numerical inversion, atmospheric parameterization and the adaptation to SeaWiFS and MODIS. POLYMER version used in this ATBD is v4.14, strictly equivalent to release v4.17 for the considered sensors.

In POLYMER, a preliminary sun glint reflectance is estimated from the Cox and Munk (1954) model relating sea surface roughness to wind speed and acquisition geometry. This contribution is tabulated simultaneously with Rayleigh scattering (including coupling between both) and contains potentially large errors due to only approximate knowledge of the wind field at pixel scale. The core of the atmospheric correction is then built upon an ocean-atmosphere radiometric model, in which coupled inversion over the full spectrum seeks to retrieve the residual sun glint, together with aerosol signal and any other atmospheric contributor (e.g. undetected thin cloud). This atmospheric and glint residual component, noted ρ_{ag}, is modelled by a function of λ consisting of three terms:

$$\rho_{ag}(\lambda, c_0, c_1, c_2) = c_0 T_0(\lambda)\lambda^{p_0} + c_1\lambda^{p_1} + c_2\rho_R(\lambda) \quad (17)$$

We refer to Steinmetz et al. (2015) for a detailed description of this modelling, where the exponents $p_0 = 0$, $p_1 = -1$ and third term in $\rho_R(\lambda)$ close to λ^{-4} are chosen to represent spectrally flat components (attenuated by a mixed direct/diffuse transmittance $T_0(\lambda)$), aerosol, and coupling with Rayleigh respectively. Coefficients (c_0, c_1, c_2) are the atmospheric unknowns. The marine model, noted ρ_w^{mod}, is inevitably required when atmospheric correction deals with wavelengths in the visible (see e.g. Bricaud and Morel (1987) for a precursor approach on CZCS). The earliest version of POLYMER relies on the Morel and Maritorena (2001) model parameterised by chlorophyll concentration, modified to also take into account backscattering of non-covarying particles and extended beyond 700 nm by the similarity spectrum of Ruddick et al. (2006). Some bio-optical constraints have been further added in Steinmetz et al. (2015), so that we shall simply keep the generic notation $\rho_w^{mod}(\lambda, \varphi)$ where φ represents a set of biological unknowns. The present analysis does not need a more explicit form, except to count the degrees of freedom, here two. In the end POLYMER relies on following TOA formulation:

$$\rho_t(\lambda) = t_g(\lambda)\left(\rho_R(\lambda) + \rho_{ag}(\lambda, c_0, c_1, c_2) + t(\lambda)\left(\rho_w^{mod}(\lambda, \varphi) + \varepsilon(\lambda)\right)\right) \quad (18)$$

Where $\varepsilon(\lambda)$ is the BOA residual resulting from inherent discrepancy between the full model and the TOA radiometry. Note that ρ_R is here a shorthand which implicitly contains the Cox and Munk sun glint (term $\rho_{mol+gli}$ in Steinmetz et al. 2011). Moreover, the diffuse transmittance $t(\lambda)$ includes only the Rayleigh part and it is thus known from auxiliary data. The actual TOA quantity involved in POLYMER optimisation is the radiometry corrected for gaseous absorption, Rayleigh and sun glint, noted ρ_{Rc} hereafter:

$$\rho_{Rc}(\lambda) = \frac{\rho_t(\lambda)}{t_g(\lambda)} - \rho_R(\lambda) \quad (19)$$

It follows that given a set of atmospheric and bio-optical parameters $(\hat{c_0}, \hat{c_1}, \hat{c_2}, \hat{\varphi})$, both terms ρ_{ag} and ρ_w^{mod} can be evaluated and marine reflectance is retrieved at any wavelength by:

$$\rho_w(\lambda) = \frac{\rho_{Rc}(\lambda) - \rho_{ag}(\lambda)}{t(\lambda)} = \rho_w^{mod}(\lambda, \hat{\varphi}) + \varepsilon(\lambda) \quad (20)$$

Importantly the second equality shows that this reflectance is also the sum of ρ_w^{mod} and the residual $\varepsilon(\lambda)$ (by definition of Eq. 18), so that POLYMER final product is not strictly speaking the output of the marine model ρ_w^{mod}. The left part of Eq. (20) differs essentially from standard atmospheric correction (Eq. (3)) in the way the ρ_{ag} term is computed. POLYMER first reduces the dimensionality of the non-linear problem by linking the atmospheric unknowns to the bio-optical unknowns. Indeed, for any ρ_w^{mod}, the coefficients can be best evaluated by minimising a linear least-square problem:

$$\begin{cases} (\hat{c_0}, \hat{c_1}, \hat{c_2}) = \underset{(c_0,c_1,c_2)}{argmin}\, \chi^2_{atm} \\ \text{with } \chi^2_{atm} = \sum_{i=1}^{n} \left(T_0(\lambda_i) c_0 {\lambda_i}^{p_0} + c_1 {\lambda_i}^{p_1} + c_2 \rho_R(\lambda_i) - \left(\rho_{Rc}(\lambda) - t(\lambda_i)\, \rho_w^{mod}(\lambda_i, \varphi)\right)\right)^2 \end{cases} \quad (21)$$

These coefficients are thus a linear combination of $\rho_w^{mod}(\lambda_i, \varphi)$ (see section 3 for an explicit formulation) and provide, through ρ_{ag}, a marine reflectance depending on φ, noted $\rho_w(\lambda, \varphi)$. Then POLYMER minimises the discrepancy between this retrieved reflectance and the marine model, with respect to the φ unknown only:

$$\hat{\varphi} = \underset{\varphi}{argmin}\, \chi^2_{bio}(\varphi) \;\text{ where }\; \chi^2_{bio}(\varphi) = \sum_{i=1}^{n} \left(\frac{\rho_w(\lambda, \varphi) - \rho_w^{mod}(\lambda_i, \varphi)}{\sqrt{\rho_w^{mod}(\lambda_i, \varphi)}} \right)^2 \quad (22)$$

Numerator of Eq. 22 is exactly the residual $\varepsilon(\lambda)$. Root square in denominator weights the cost function according to the amplitude of the marine signal at different wavelengths (with a threshold of 0.005, not made explicit here). The spectral coupling over the full spectrum appears clearly in minimisation of cost functions χ^2_{atm} and χ^2_{bio}, built upon all available n bands of the sensor.

In situ database

The single source of in-situ data considered for present vicarious calibration is the Marine Optical BuoY (MOBY), whose data have been used for decades by space agencies. On top of its high quality and appropriateness for vicarious calibration (e.g. Zibordi et al. 2015), the MOBY dataset has the rare advantage of exhibiting systematic measurements at all visible bands of all sensors, what is strictly required in the present context of spectrally coupled atmospheric correction. This is achieved by integration of the raw hyperspectral measurements against each sensor spectral response function (RSF). So-called “GOLD” and “Platinum” datasets were downloaded by PML. MOBY GOLD data are available up to May 2022 for 6 sensors (Aqua-MODIS, MERIS, Suomi-VIIRS, NOAA-20-VIIRS, OLCI-A, and OLCI-B). MOBY Platinum started in May 2024, and for this dataset only 4 sensors are available (Suomi-VIIRS, NOAA-20-VIIRS, OLCI-A, and OLCI-B). We emphasize that only Platinum data over Hawaii were considered for the SVC.

For independent validation, we use MarONet data in Australia (off Perth), where waters are not as clear as over Hawaii. Another independent dataset for assessing the impact of SVC over diverse coastal waters is the Ocean Colour component of the Aerosol Robotic Network (AERONET-OC, Zibordi et al. 2009b); currently, we consider only the Aqua-Alta Oceanographic Tower in the northern Adriatic Sea (AAOT, Zibordi et al. 2004). Note that no band-shift is applied at this stage.

For all sites, the normalisation procedure follows Park and Ruddick (2005), because it corresponds exactly to the BRDF model used by POLYMER (consistency between in situ and satellite data).

Satellite data and match-up building

Six ocean colour sensors are considered and listed in *Table 1*. Level-1 data are exempt of any space agency’s vicarious calibration. MODIS and VIIRS data are first corrected for polarisation (this is done in POLYMER, with polarisation coefficients). The OC-CCI satellite archive was extracted by PML over the coincident in situ data, and forms the so-called match-up database (MDB). The meteorological ancillary data used in POLYMER processing comes most recent ECMWF reanalysis (ERA5).

Table 1. List of sensors and L1 data used for SVC

Sensor short name	Platform	Level	Processing version	Resolution at nadir	Time range (approximate)
MERIS	ENVISAT	Level-1b	ESA 4th reprocessing	1.2 km (RR)	2002-2012
MODIS	Aqua	Level-1C	NASA latest reprocessing	1 km	2002-2022
OLCI-A	Sentinel-3A	Level-1b	EUMETSAT baseline OL__L1_.004.00.00	300 m (FR)	2016-2022 & 2024-2025
OLCI-B	Sentinel-3B	Level-1b	EUMETSAT baseline OL__L1_.004.00.00	300 m (FR)	2018-2022 & 2024-2025
VIIRSN	S-NPP	Level-1C	NASA latest reprocessing	750 m	2012-2022 & 2024-2025
VIIRSJ1	JPSS1	Level-1C	NASA latest reprocessing	750 m	2018-2022 & 2024-2025

For vicarious gain computation and pixel-by-pixel verification at MOBY, we follow as much as possible protocols of the standard SVC defined in Franz et al. (2007): time difference between satellite and ground measurement less than three hours, sun zenith angle less than 70°, view zenith angle less than 56°, 5x5 macro-pixel extractions around the in-situ point without any flagged pixel. Due to its robustness, POLYMER is quite permissive in the data screening and provides few quality flags. Hence only pixels flagged by POLYMER as cloud or with an explicit atmospheric correction failure are discarded (negative particulate backscattering, out of bound parameters in the minimisation). There was no screening based on chlorophyll concentration, expected to be very low at MOBY. After careful consideration, pixels impacted by sun glint have been kept as valid because of POLYMER's capability to well perform under such condition and because such data are considered in the Level-2 OC-CCI dataset.

Numerical method

We first introduce vector and matrix notation to deal more easily with the spectral dimension. Unless explicitly mentioned, the dimension is n (number of bands used in the atmospheric correction) and we note:

$$\rho = \begin{pmatrix} \rho(\lambda_1) \\ \vdots \\ \rho(\lambda_n) \end{pmatrix} \tag{23}$$

For the sake of readability, we start by studying the optimisation problem of Eq. (12) in the simple case $l = m = n$, and will deal with the general case just after. Let us call F the function relating vicarious gains to the retrieved marine reflectance:

$$\begin{array}{llc} F: \mathbb{R}^n & \to & \mathbb{R}^n \\ g & \to & F(g) = \begin{pmatrix} f_1\left(g_1 * \rho_t(\lambda_1), \cdots, g_n * \rho_t(\lambda_n)\right) \\ \vdots \end{pmatrix} \end{array} \tag{24}$$

This is just another writing of functions f_i, directly expressed with respect to gains instead of TOA radiometry. In particular, we have $F(1) = \rho_{wN}$, i.e. the marine reflectance without any vicarious calibration. The cost function then simply writes $\chi^2_{SVC}(g) = \| \rho^t_{wN} - F(g) \|^2$ and its minimum is solution of the $n \times n$ non-linear system

$$\nabla F'(\rho^t_{wN} - F(g)) = 0 \tag{25}$$

Where ∇F is the Jacobian matrix of F, evaluated at current g, and the prime superscript stands for its transpose. There is an obvious link between ∇F and the Jacobian matrix J of function f previously defined in Eq. (10); notably for $g = 1$ we have:

$$\nabla F(1) = \begin{pmatrix} \rho_t(\lambda_1)\frac{\partial \rho_{wN}(\lambda_1)}{\partial \rho_t(\lambda_1)} & \cdots & \rho_t(\lambda_n)\frac{\partial \rho_{wN}(\lambda_1)}{\partial \rho_t(\lambda_n)} \\ \vdots & \ddots & \vdots \\ \rho_t(\lambda_1)\frac{\partial \rho_{wN}(\lambda_n)}{\partial \rho_t(\lambda_1)} & \cdots & \rho_t(\lambda_n)\frac{\partial \rho_{wN}(\lambda_n)}{\partial \rho_t(\lambda_n)} \end{pmatrix} \tag{26}$$

Such system can only be solved numerically, especially if the atmospheric correction of concern is not explicit. Any standard computational method can be candidate, albeit it requires iterative runs of the atmospheric correction, on a pixel-per-pixel basis. By default, we propose here a one-step inversion, based on the fact that calibration gains are expected to be small with respect to unity, typically less than 5%. Any larger value would originate from a major problem in either the instrumental calibration or the atmospheric correction itself, and would need a dedicated correction beyond the scope of vicarious calibration. It is worth noting that iteration around the step described hereafter is still possible in our code.

A first order Taylor expansion around $g = 1$ writes $F(g) \approx F(1) + \nabla F(1)(g-1)$ and allows Eq. (25) to be solved approximately with the $n \times n$ linear system:

$$\nabla F' \nabla F(g-1) = \nabla F'(\rho_{wN}^t - \rho_{wN}) \tag{27}$$

Here ∇F is implicitly defined at $g = 1$. This solution can be interpreted as the first iteration of the Gauss-Newton algorithm minimising χ^2_{SVC}. Now, when dealing with the general case of gains retrieval for l bands only, with a cost function defined on m bands with $l \leq m \leq n$, the very same algebra is true when considering in Eq. (27) the $m \times l$ submatrix of ∇F and restricting $\rho_{wN}^t - \rho_{wN}$ to m rows. Due to multiplication with matrix $\nabla F'$, Eq. (27) is then simply a $l \times l$ linear system. Such solver is used hereafter in section 4 for SeaWiFS, MODIS and MERIS, with details on the band sets for each sensor.

Note that if the strict SVC were possible, with an equal number of unknowns and equations ($l = m$), Eq. (27) would be equivalent to the linear system $\nabla F(g-1) = \rho_{wN}^t - \rho_{wN}$, which now would be interpreted as the first iteration of the Newton-Raphson algorithm to solve the strict problem $F(g) = \rho_{wN}^t$. It follows that our solution is exact for a linear atmospheric correction (with respect to the TOA radiometry); it is indeed an easy exercise to check that it retrieves exactly the standard gains when applied to the standard atmospheric correction, cf. Eqs. (14)-(15)-(16). In this respect we can see the solution of Eq. (27) as a natural generalisation of the standard gain computation Eqs. (5)-(7). Furthermore, the linear system highlights, at first order, the spectral coupling between gains through the Jacobian matrix.

For an algorithm such as POLYMER, when the aerosol component is not analytically given, partial derivatives must be approximated numerically. We use a second order approximation, to have more accuracy in the Jacobian matrix than in the inverse method itself:

$$\frac{\partial f_i}{\partial x_j} \approx \frac{f_i(x_1, \cdots, x_j + h_j, \cdots, x_n) - f_i(x_1, \cdots, x_j - h_j, \cdots, x_n)}{2h_j} \quad \text{with } h_j \ll 1 \tag{28}$$

In practice for each calibration scene, these terms are computed by applying POLYMER on $2 * l$ Level1 modified scenes whose TOA signal are $\rho_t(\lambda_j) \pm h_j$ for $j = 1 \dots l$. Note again that this approximate scheme gives exactly the expected vicarious gains for a linear atmospheric correction decoupling all bands. The choice of step h_j depends on how quickly f_i varies with respect to x_j. Numerical tests have convinced us to consider a relative step instead of an absolute step, i.e. $h_j = s * \rho_t(\lambda_j)$. Another advantage is that because of the $\rho_t(\lambda_i)$ factor in Eq. (26), a relative step allows to use either TOA radiance and reflectance as the input variable:

$$L_t \frac{\partial \rho_w(L_t)}{\partial L_t} = \rho_t \frac{\partial \rho_w(\rho_t)}{\partial \rho_t} \tag{29}$$

While we have here described the formalism in term of ρ_t, in practice radiance L_t is used, as it is provided in the Level 1 products. Several trials for various relative steps (from 0.05% to 5%) show that s =0.5% or 1% gives a good approximation of the derivative at every wavelength. This is illustrated on Figure 3 for $\frac{\partial \rho_w(443)}{\partial \rho_t(560)}$:

the 0.5% differentiation has the closest numerical derivative to the exact derivative computed by spline interpolation. It is noteworthy that increments that are too small yield to totally erroneous values because then numerical differences reach the limit of numerical accuracy and become meaningless.

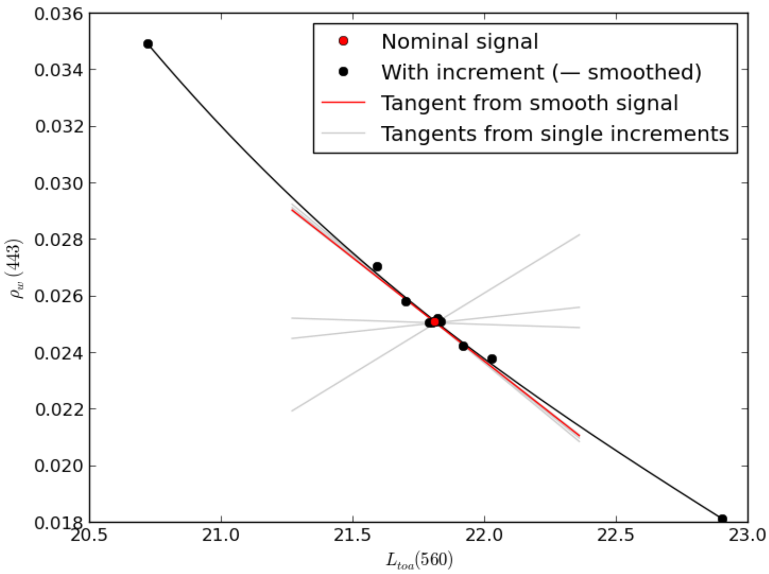

Figure 3. Example of numerical differentiation of $\rho_w(443)$ by $L_t(560)$. The red dot corresponds to nominal signal and ten black dots for modified $L_t(560)$ with step ±5%, ±1%, ±0.5%, ±0.1% and ±0.05% (ordered on the x-axis). Numerical derivative for each step is represented by the tangent lines in grey. The true derivative is computed by spline interpolation and represented by the tangent red line.

To sum up, our numerical method defined by Eqs. (27)-(28) is based on the sole approximation of a first order expansion. Validity of this reduction is directly linked to the degree of linearity of the atmospheric correction with respect to radiometry. We remind that our code allows for more iterations, if needed. Practically, suitability of the computed individual gains is checked a posteriori, on pixel-by-pixel calibrated data. For all subsequent analysis (plots, statistics, averaging…), we only keep individual gain which allow to retrieve the in situ reflectance within $5x10^{-4}$.

Eventually, the gain averaging needs to be explained. Due to the spectral coupling, individual gains for a certain match-up point are only meaningful when defined spectrally. In order to keep this spectral consistency in the mean gains (first per match-up and then per mission), we thus apply the MSIQR of Eq. (8) simultaneously for all calibrated bands. In other words, the spatial (respectively temporal) mean is computed on the same pixels (respectively same match-ups) for all wavelengths. This generally results in a more severe screening than the band-per-band MSIQR: if some gain spectra differ too much from the mean shape, the mean may be based on less than 50% of the initial data.

Decoupled step

In some cases, non-standard AC may decouple a subset of the bands, which then may be calibrated with the standard SVC method. Typically, POLYMER uses m bands λ_i (ordered previously with indices $1 \leq i \leq m$) to retrieve the unknown atmospheric parameters (c_0, c_1, c_2), from which the atmospheric term $\rho_{ag}(\lambda_k)$ and the marine reflectance $\rho_w(\lambda_k)$ can be computed at any other band λ_k not involved in the inversion $(k > m)$, thanks to Eqs. (17)-Eq.(18). It follows that band λ_k is fully decoupled from the aerosol detection and can be calibrated independently. More generally, a set of decoupled bands can be calibrated at once, as for standard AC, where the Jacobian matrix is diagonal. Practically, we achieve this calibration by the very same code, in a second step, i.e. after application of the averaged (coupled) gains. This situation potentially concerns bands 681 & 709 nm for MERIS, 400, 412, 681 & 709 nm for OLCI and 410 nm for VIIRS, assuming in situ data are provided.

3. Theoretical analysis of POLYMER vicarious calibration

Multiplicity of vicarious gains

We start by rewriting the POLYMER algorithm in a more compact form, using the vector and matrix notation. First, the atmospheric term ρ_{ag} defined by Eq. (17) depends linearly on the coefficients (c_0, c_1, c_2) through

$$\begin{pmatrix}\rho_{ag}\\ \vdots\end{pmatrix} = \Lambda \begin{pmatrix}c_0\\ c_1\\ c_2\end{pmatrix} \quad \text{where } \Lambda = \begin{pmatrix}T_0(\lambda_1){\lambda_1}^{p_0} & {\lambda_1}^{p_1} & \rho_R(\lambda_1)\\ \vdots & \vdots & \vdots\\ T_0(\lambda_n){\lambda_n}^{p_0} & {\lambda_n}^{p_1} & \rho_R(\lambda_n)\end{pmatrix} \tag{30}$$

Matrix Λ is rectangular, of size $n \times 3$, and computed once for each pixel. Thus the over constrained least-square minimisation of Eq. (21) writes:

$$\chi^2_{atm}(c_0, c_1, c_2) = \left\| \Lambda \begin{pmatrix}c_0\\ c_1\\ c_2\end{pmatrix} - \begin{pmatrix}\rho_{Rc} - t\,\rho_w^{mod}(\varphi)\\ \vdots\end{pmatrix} \right\|^2 \tag{31}$$

Solution is given by introducing the pseudo-inverse matrix of Λ:

$$\begin{pmatrix}c_0\\ c_1\\ c_2\end{pmatrix} = (\Lambda'\Lambda)^{-1}\Lambda' \begin{pmatrix}\rho_{Rc} - t\,\rho_w^{mod}(\varphi)\\ \vdots\end{pmatrix} \tag{32}$$

Secondly, let us introduce the square $n \times n$ matrix M by

$$M = I - \Lambda(\Lambda'\Lambda)^{-1}\Lambda' \tag{33}$$

Then the whole POLYMER optimisation problem Eq. (22) and associated marine reflectance Eq. (20) can be summarised by

$$\begin{cases} \begin{pmatrix}t\rho_w\\ \vdots\end{pmatrix} = \begin{pmatrix}t\,\rho_w^{mod}(\hat{\varphi})\\ \vdots\end{pmatrix} + M \begin{pmatrix}\rho_{Rc} - t\,\rho_w^{mod}(\hat{\varphi})\\ \vdots\end{pmatrix} \\ \hat{\varphi} = \underset{\varphi}{argmin}\, \chi^2_{bio}(\varphi) \quad \text{where } \chi^2_{bio}(\varphi) = \left\| \dfrac{M \begin{pmatrix}\rho_{Rc} - t\,\rho_w^{mod}(\varphi)\\ \vdots\end{pmatrix}}{t\sqrt{\rho_w^{mod}(\varphi)}} \right\|^2 \end{cases} \tag{34}$$

Marine reflectance is here provided at TOA for the sake of simplicity, what is equivalent to BOA since diffuse transmittance does not depend on the inversion. Eq. (34) gives a direct insight in POLYMER spectral coupling by matrix M, through both the definition of ρ_w (top equation) and the determination of $\hat{\varphi}$ (bottom equation).

A key feature of matrix M is to be singular, and more precisely that its kernel is of dimension 3. Indeed, for any triplet (x_0, x_1, x_2), we have

$$M\Lambda \begin{pmatrix}x_0\\ x_1\\ x_2\end{pmatrix} = (\Lambda - \Lambda(\Lambda'\Lambda)^{-1}\Lambda'\Lambda) \begin{pmatrix}x_0\\ x_1\\ x_2\end{pmatrix} = \begin{pmatrix}0\\ \vdots\end{pmatrix} \tag{35}$$

This has direct implication for vicarious calibration. For any (x_0, x_1, x_2), we define specific gains by

$$g(\lambda) = 1 + t_g(\lambda)\frac{x_0 T_0(\lambda)\lambda^{p_0} + x_1\lambda^{p_1} + x_2\rho_R(\lambda)}{\rho_t(\lambda)} \tag{36}$$

By construction, applying these gains at TOA yields to a new Rayleigh-corrected signal which satisfies (we here used the cal superscript for all quantities after vicarious calibration):

$$\begin{pmatrix}\rho_{Rc}^{cal}\\ \vdots\end{pmatrix} = \begin{pmatrix}\rho_{Rc}\\ \vdots\end{pmatrix} + \Lambda \begin{pmatrix}x_0\\ x_1\\ x_2\end{pmatrix} \tag{37}$$

Following Eqs. (34) and (35), this leads to the very same solution: $\rho_w^{cal} = \rho_w$ and $\hat{\varphi}^{cal} = \hat{\varphi}$. Hence POLYMER is insensitive to any gain which effect is to add an aerosol contribution. More generally, given some hypothetical vicarious gains independently derived for POLYMER, this algebra demonstrates that there is a multiplicity of equivalent calibrations by addition of any spectral shape as in Eq. (36). Very importantly, equivalence between all these calibrations is true only when this equation is applied to all bands involved in the atmospheric correction. At first sight this property is striking, in comparison with the usual experience of vicarious calibration which classically defines unique gains by Eq. (5); the standard case is however more complex than it appears to be and is further discussed in section5.

Let us give a tangible illustration, by comparing a standard POLYMER run on MODIS at MOBY with two others after application of some specific gains. Instead of fixing coefficients (x_0, x_1, x_2), which meaning is not straightforward, we can equivalently define three gains at three wavelengths, then deduce the coefficients by solving the linear system

$$\Lambda_{[\lambda_1,\lambda_2,\lambda_3]} \begin{pmatrix} x_0 \\ x_1 \\ x_2 \end{pmatrix} = \begin{pmatrix} (g(\lambda_1) - 1)\dfrac{\rho_t}{t_g}(\lambda_1) \\ (g(\lambda_2) - 1)\dfrac{\rho_t}{t_g}(\lambda_2) \\ (g(\lambda_3) - 1)\dfrac{\rho_t}{t_g}(\lambda_3) \end{pmatrix} \quad (38)$$

Where $\Lambda_{[\lambda_1,\lambda_2,\lambda_3]}$ is the 3×3 submatrix of Λ restricted to lines λ_1, λ_2, and λ_3. We take here two examples differing significantly in their spectral shapes: first we fix $g(412) = 1.02$, $g(488) = 1.01$ and $g(667) = 0.99$; then we fix $g(412) = 0.97$, $g(488) = 0.99$ and $g(667) = 1.02$. In each case, solving Eq. (38) gives the three coefficients, then providing gains at all other wavelengths through Eq. (36). All individual gains of all match-ups are plotted on Figure 4 (left), on top and bottom row for the two examples respectively. Gains differ a priori for each pixel due to the ρ_t/t_g term, yet they appear here very stable in the visible bands, where they are forced to match three unique values. The associated marine reflectance is provided on middle and right side of Figure 4 at 412 and 488 nm respectively, in comparison with the non-calibrated case. The perfect match illustrates numerically our theoretical findings.

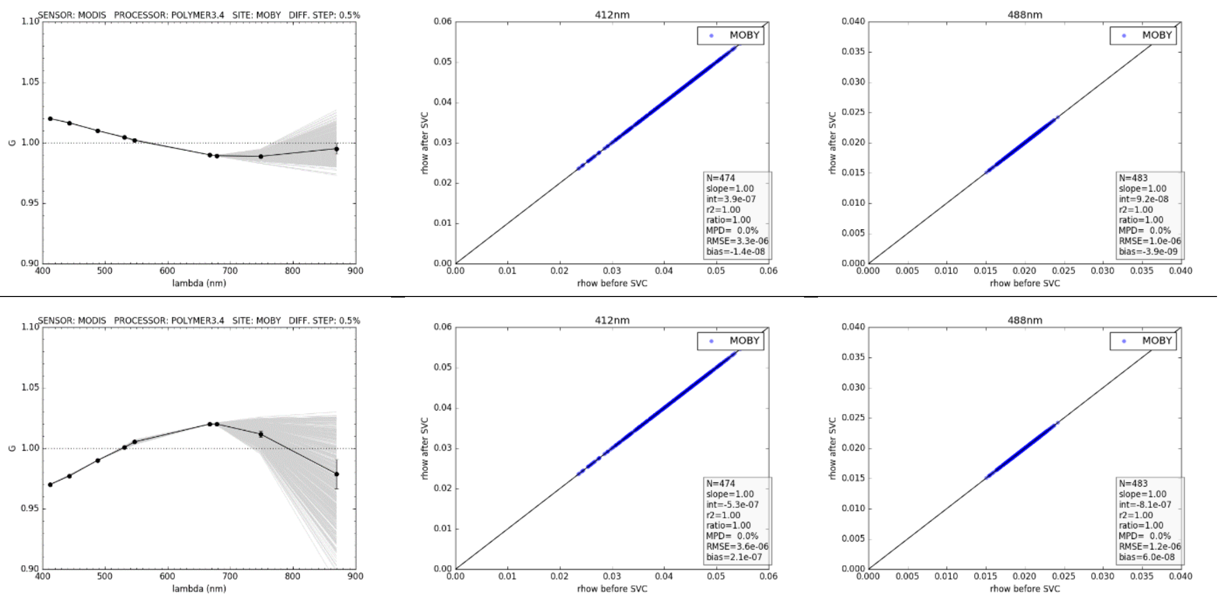

Figure 4. Individual gains computed artificially for MODIS at MOBY from Eq. (30) (left, grey curves; black curve is the average gain) in two cases (top and bottom rows, see text for values) and the associated retrieval of $\rho_w(412)$ (middle, y-axis) and $\rho_w(488)$ (right, y-axis) compared to the nominal ρ_w without calibration (x-axis).

As a consequence, POLYMER gains have no absolute meaning per se; in particular, gains with large amplitude may have exactly the same effect as a very small calibration. The key parameter is the shape of the gains, after removal of the aerosol and residual glint component. This property can be used to filter the gain spectra and find the shape with lowest dispersion around unity. From a numerical point of view, multiplicity of solution may lead to instability in the inversion. A solution to circumvent this issue is to fix three gains (to any values), what set the aerosol component to a given level (as in Eq. 38). Hence, when POLYMER uses n bands in the AC, our numerical method computes gains at only $n-3$ bands. Practical details for each sensor are given in section 4.

Impossibility of a strict SVC

As already defined in Eq. (11), the strict SVC aims at forcing the processor to exactly match the in-situ data, on a pixel-per-pixel basis. We here consider in-situ reflectance ρ_w^t converted to the geometry of the pixel, as done in practice by the standard SVC, in order to directly use POLYMER formulation of Eq. (34) in the sensor geometry. The vicarious gain $g = (g(\lambda_1), \ldots, g(\lambda_n))$ is unequivocally related to $\rho_{Rc}^{cal}(g) = g * \rho_t / t_g - \rho_R$ which by definition of SVC must satisfy:

$$\begin{cases} M\begin{pmatrix}\rho_{Rc}^{cal}(g) - t\,\rho_w^{mod}(\hat{\varphi}(g)) \\ \vdots\end{pmatrix} = \begin{pmatrix} t\rho_w^t - t\,\rho_w^{mod}(\hat{\varphi}(g)) \\ \vdots \end{pmatrix} \\ \text{where } \hat{\varphi}(g) = \underset{\varphi}{argmin} \left\| \frac{M\begin{pmatrix}\rho_{Rc}^{cal}(g) - t\,\rho_w^{mod}(\varphi) \\ \vdots\end{pmatrix}}{t\sqrt{\rho_w^{mod}(\varphi)}} \right\|^2 \end{cases} \tag{39}$$

Here it is important to note the dependency of retrieved bio-optical unknown $\hat{\varphi}$ on the gain itself. Because M is not invertible, the necessary condition for the first equation to be solved it that it exists a vector X, a priori dependent on g, such that

$$t\rho_w^t - t\,\rho_w^{mod}(\hat{\varphi}(g)) = MX(g) \tag{40}$$

In this case, gains are solution of the non-linear system

$$\rho_{Rc}^{cal}(g) = X(g) + t\,\rho_w^{mod}(\hat{\varphi}(g)) + \Lambda\begin{pmatrix}x_0 \\ x_1 \\ x_2\end{pmatrix} \tag{41}$$

The last term comes from the multiplicity of gains with any aerosol term defined by (x_0, x_1, x_2).

In such case, the POLYMER cost function is evaluated as

$$\chi_{bio}^2(\varphi) = \left\| \frac{M\begin{pmatrix}X(g) + t\,\rho_w^{mod}(\hat{\varphi}(g)) - t\,\rho_w^{mod}(\varphi) \\ \vdots\end{pmatrix}}{t\sqrt{\rho_w^{mod}(\varphi)}} \right\|^2 \tag{42}$$

Now we use the fact that $M * M = M$ (this is a trivial check from definition of Eq. (33)), so that we have

$$MX(g) = M\big(t\rho_w^t - t\,\rho_w^{mod}(\hat{\varphi}(g))\big) \tag{43}$$

POLYMER solution is thus given by

$$\hat{\varphi}(g) = \underset{\varphi}{argmin} \left\| \frac{M\begin{pmatrix}t\rho_w^t - t\,\rho_w^{mod}(\varphi) \\ \vdots\end{pmatrix}}{t\sqrt{\rho_w^{mod}(\varphi)}} \right\|^2 \tag{44}$$

This shows that $\hat{\varphi}(g)$ does in fact not depend on g. The minimum of POLYMER cost function is simply reached for $\hat{\varphi}$ which best fits the in-situ data (in the POLYMER norm). It follows that X, which is related through matrix M to the discrepancy between the in-situ signal and the modelled reflectance retrieved by POLYMER, does not depend on g either. Then, because M is built upon atmospheric terms totally independent of any marine model, it is physically only relevant to restrict X to zero and understand Eq. (40) as:

$$t\rho_w^t = t\,\rho_w^{mod}(\hat{\varphi}) \tag{45}$$

In such case, we recognize in Eq.(41) the very same definition of gain as in the standard case, written for any POLYMER aerosol reflectance:

$$g(\lambda) = \frac{t_g(\lambda)\big(t(\lambda)\rho_w^t(\lambda) + \rho_R(\lambda) + x_0 T_0(\lambda)\lambda^{p_0} + x_1\lambda^{p_1} + x_2\rho_R(\lambda)\big)}{\rho_t(\lambda)} \tag{46}$$

Interestingly this means that, in such very particular condition, POLYMER SVC can be solved analytically; at first sight Eq. (46) could appear as spectrally-decoupled, but we must remind that the coupling is done implicitly through the marine model since one has $\rho_w^t(\lambda) = \rho_w^{mod}(\hat{\varphi}, \lambda)$ for all bands.

This analysis demonstrates that the strict SVC problem can only be solved if the marine model embedded in POLYMER manages to exactly match the in-situ measurement, for some bio-optical parameters, Eq.(45). In practice there is obviously no chance to meet such condition. We can a posteriori check that applying gains of Eq. (46) does not force POLYMER to exactly retrieve ρ_w^t, as can be seen on scatter plots of Figure 5, despite a noticeable improvement.

This fundamental finding, associated to the multiplicity of solution (previous section), explains why trying to solve the strict SVC problem leads to numerical instability and erroneous solution, variable with the chosen bands set (results not shown here).

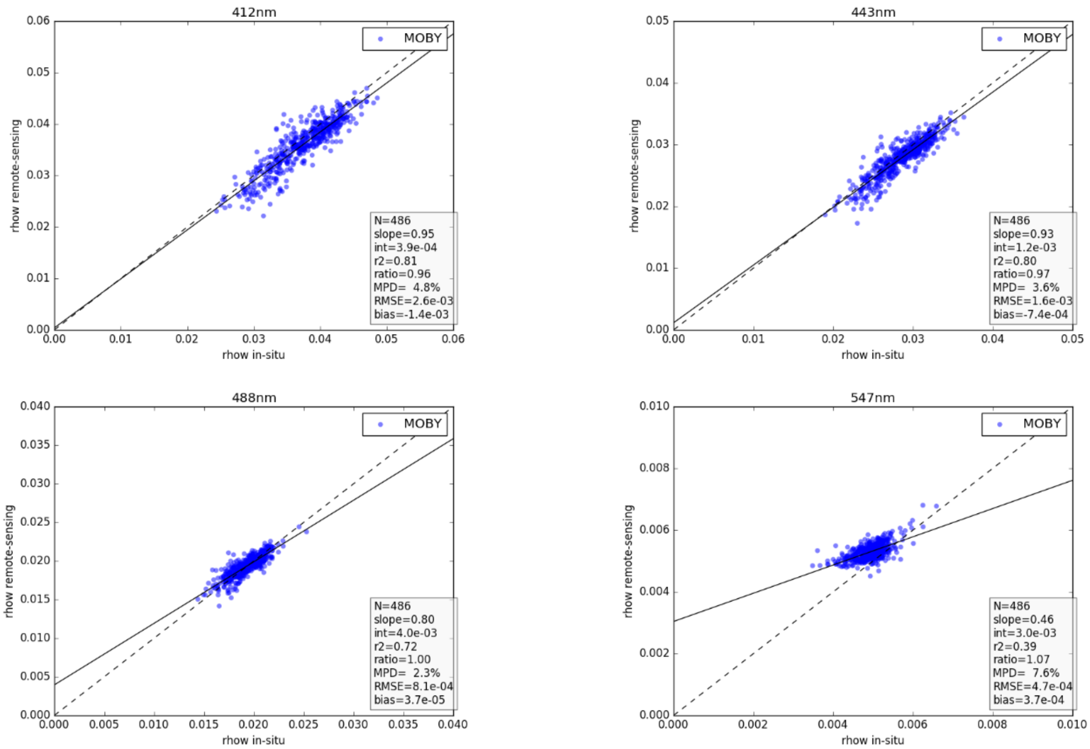

Figure 5. Validation of MODIS ρ_w at MOBY after applying standard pixel-by-pixel vicarious gains, defined by Eq. (47). Bands are 412, 443, 488 and 547 nm from top to bottom and left to right.

Optimal SVC

Now that we have demonstrated that a strict SVC is not possible, we can study the optimal SVC, as introduced and defined in Eq. (12). Its application to POLYMER means that we search for a gain $\hat{g}$ solution of this minimisation problem:

$$\begin{cases} \hat{g} = \underset{g}{argmin}\ \chi^2_{SVC}(g) \\ \text{where } \chi^2_{SVC}(g) = \left\| \dfrac{M\begin{pmatrix}\rho^{cal}_{Rc}(g) - t\,\rho^{mod}_w(\hat{\varphi}(g)) \\ \vdots \end{pmatrix} - \begin{pmatrix} t\rho^t_w - t\,\rho^{mod}_w(\hat{\varphi}(g)) \\ \vdots \end{pmatrix}}{t} \right\|^2 \\ \text{and } \hat{\varphi}(g) = \underset{\varphi}{argmin}\ \chi^2_{bio}(\varphi, g) \ \text{ with } \ \chi^2_{bio}(\varphi, g) = \left\| \dfrac{M\begin{pmatrix}\rho^{cal}_{Rc}(g) - t\,\rho^{mod}_w(\varphi) \\ \vdots \end{pmatrix}}{t\sqrt{\rho^{mod}_w(\varphi)}} \right\|^2 \end{cases} \tag{47}$$

The hat accent is here added to the optimal gain, to avoid any confusion with the free variable in $\chi^2_{SVC}(g)$. Note also in this cost function the division by transmittance, aiming at best matching the in-situ reflectance at sea level. Dimensions of vectors being here implicit, we remind that in the most general case, summation runs over n bands in χ^2_{bio} (POLYMER inversion), m bands in χ^2_{SVC} and that g is defined on l bands (the other ones being set to unity) with $l \leq m \leq n$. Eq. (47) is a coupled minimisation problem in the two free variables g and φ, defining POLYMER individual gains in an optimal sense. Its exact resolution is beyond our reach and justifies the use of a numerical method such as that one introduced in section 2.

To seize in more concrete terms the optimal SVC, we can deal with a slightly modified and more tractable version of POLYMER, allowing a direct resolution of Eq. (47). In this simplified version, the output of POLYMER is set to the marine model only, without adding the residual term. This means Eq. (20) is replaced by $\rho_w(\lambda) = \rho^{mod}_w(\lambda, \hat{\varphi})$, while the whole inversion process is unchanged and retrieves identical POLYMER bio-optical parameter $\hat{\varphi}$ and aerosol content. The associated optimal SVC problem writes:

$$\begin{cases} \hat{g} = \underset{g}{argmin}\ \chi^2_{SVC\_nores}(g) \\ \text{where } \chi^2_{SVC\_nores}(g) = \|\ \rho^{mod}_w(\hat{\varphi}(g)) - \rho^t_w \|^2 \\ \text{and } \hat{\varphi}(g) = \underset{\varphi}{argmin}\ \chi^2_{bio}(\varphi, g) \ \text{ with } \ \chi^2_{bio}(\varphi, g) = \left\| \dfrac{M\begin{pmatrix}\rho^{cal}_{Rc}(g) - t\,\rho^{mod}_w(\varphi) \\ \vdots \end{pmatrix}}{t\sqrt{\rho^{mod}_w(\varphi)}} \right\|^2 \end{cases} \tag{48}$$

Interest of the new cost function $\chi^2_{SVC\_nores}$ is to discard the term related to residual, although the full spectral coupling remains in χ^2_{bio}. We can show that solution of Eq. (48) is explicitly given by

$$\hat{g}(\lambda) = \frac{t_g(\lambda)\big(t(\lambda)\,\rho^{mod}_w(\varphi^t, \lambda) + \rho_R(\lambda) + x_0 T_0(\lambda)\lambda^{p_0} + x_1\lambda^{p_1} + x_2\rho_R(\lambda)\big)}{\rho_t(\lambda)} \tag{49}$$

Where the aerosol term is, as previously, computed for any (x_0, x_1, x_2) and where φ^t provides the best match between the model and the in-situ data:

$$\varphi^t = \underset{\varphi}{argmin} \|\ \rho^{mod}_w(\varphi) - \rho^t_w \|^2 \tag{50}$$

Indeed, it is clear that $\underset{\varphi}{min}\|\ \rho^{mod}_w(\varphi) - \rho^t_w\|^2 \leq \left\|\ \rho^{mod}_w\big(\hat{\varphi}(g)\big) - \rho^t_w\right\|^2$ so that $\|\ \rho^{mod}_w(\varphi^t) - \rho^t_w\|^2$ is a lower bound of $\chi^2_{SVC\_nores}(g)$. Then choosing $\hat{g}$ as in Eq. (49) yields to $\rho^{cal}_{Rc}(\hat{g}) = t\rho^{mod}_w(\varphi^t)$, so that minimisation of χ^2_{bio} gives trivially $\hat{\varphi}(\hat{g}) = \varphi^t$, and $\chi^2_{SVC\_nores}(\hat{g}) = \|\ \rho^{mod}_w(\varphi^t) - \rho^t_w\|^2$. This lower bound being reached, it means that it is the minimum, what ends the proof. It is remarkable that optimal gain of Eq. (49) looks very similar to the standard vicarious gain definition (see e.g. Eq. (46) when the strict SVC is hypothetically possible), except that the in-situ reflectance is not directly used to reconstruct the TOA targeted signal. The spectral coupling in the vicarious gain appears once again through the $\rho^{mod}_w(\varphi^t, \lambda)$ term. Furthermore, this coupling is fully non-linear with respect to TOA radiometry, as the linear contribution ρ_t/t_g of Eqs. (19)-(20) is here not applicable. By construction, applying such vicarious gains yields to a marine signal equal to $\rho^{mod}_w(\varphi^t)$, which is not strictly matching the in-situ data; the discrepancy between both, $\Delta\,\rho^{mod}_w$, is the residual of minimisation Eq. (50):

$$\Delta\, \rho_w^{mod}(\lambda) = \rho_w^{mod}(\varphi^t, \lambda) - \rho_w^t(\lambda) \quad (51)$$

This term appears to be most informative for understanding imperfection of the marine model on the calibration site and assessing the bias that cannot be corrected by the SVC.

To conclude this section, we insist on the fact that gains of Eq. (49) do not apply to the real POLYMER algorithm because of the significant role of residual in the final marine reflectance. Hence, despite its theoretical interest, the simplified formulation of Eq. (48) is no longer considered in coming results.

4. Results: SVC gains

The following sections presents gains computed for the six sensors considered in this study. In each case, we detail:

- The configuration in term of bands for SVC. The theoretical analysis has shown that 3 bands need to be fixed to remove the ambiguity in the inversion, and they are here selected in the NIR (somehow arbitrarily). In some case, a 2nd decoupled step can be done.
- The statistics and plots of the averaged gains: number of match-ups N, averaged gains $\bar{g}$ and standard-deviation σ. We also provide the Relative Standard Error of the Mean (RSEM) proposed by Zibordi et al. (2015), which is an interesting indicator to check the suitability of gains with respect to stability requirement in ocean colour (0.5% on marine reflectance over a decade. For a given band λ_i it is computed by:

$$RSEM(\lambda_i) = \frac{\sigma(\lambda_i)}{\bar{g}(\lambda_i)} \Big/ \sqrt{N_y}$$

  Where N_y is the number of individual gains (i.e. good match-ups), scaled over a decade, i.e. $N_y = 10\ N/Y$ where Y is the number of measurement years.
- Validation plots before and when applying the individual gains per matchup, to show their relevance and limit; we remind this is done after screening, hence limited to match-ups where gains allow POLYMER to best match the in-situ data. We emphasise that application of individual gains is a theoretical exercise to get confidence in the necessarily approximated SVC for not standard AC, and that it does not inform about relevance of mission average gains.

MERIS gains

The choice of bands for SVC of MERIS is given in *Table 2*. Only bands relevant for POLYMER are provided (i.e. not absorption bands, not used in the AC nor available at Level-2). Three bands are fixed in the NIR and seven bands are handled in the coupled SVC. Bands 681 and 709 nm are calibrated in the second decoupled step.

Table 2. POLYMER & SVC band set configuration for MERIS.

Sensor bands (Level-2 output)	Used in AC	Fixed for SVC	Used for SVC – coupled step	Used for SVC – decoupled step
412	✓		✓	
443	✓		✓	
490	✓		✓	
510	✓		✓	
560	✓		✓	
620	✓		✓	
665	✓		✓	
681				✓
709				✓
754	✓	✓		
779	✓	✓		
865	✓	✓		

MERIS average gains are provided in Table 3 and spectral shapes of all individual gains are displayed on Figure 6. Time-series of individual gains are provided in *Figure 7*. Validation before and after individual gains is shown in *Figure 8*, only for gains actually selected in the averaging process, and demonstrates that the individual gains perfectly make sense for all bands (only noise is visible in the red, where the signal is extremely low for such oligotrophic waters).

Table 3. Averaged POLYMER vicarious gains derived for MERIS at MOBY. Asterisk stands for fixed gains.

Band	N	$\overline{g}$	σ	RSEM
412	96	1.015955	0.018419	0.001821
443	96	1.012668	0.015077	0.001495
490	96	0.99911	0.009998	0.001005
510	96	0.997717	0.009297	0.000936
560	96	0.985534	0.006831	0.000696
620	96	0.985615	0.006128	0.000624
665	96	0.982342	0.00586	0.000599
681	259	0.981968	0.000978	0.000061
709	259	1.021344	0.007793	0.000470
754	NA	$1^{(*)}$	NA	NA
779	NA	$1^{(*)}$	NA	NA
865	NA	$1^{(*)}$	NA	NA

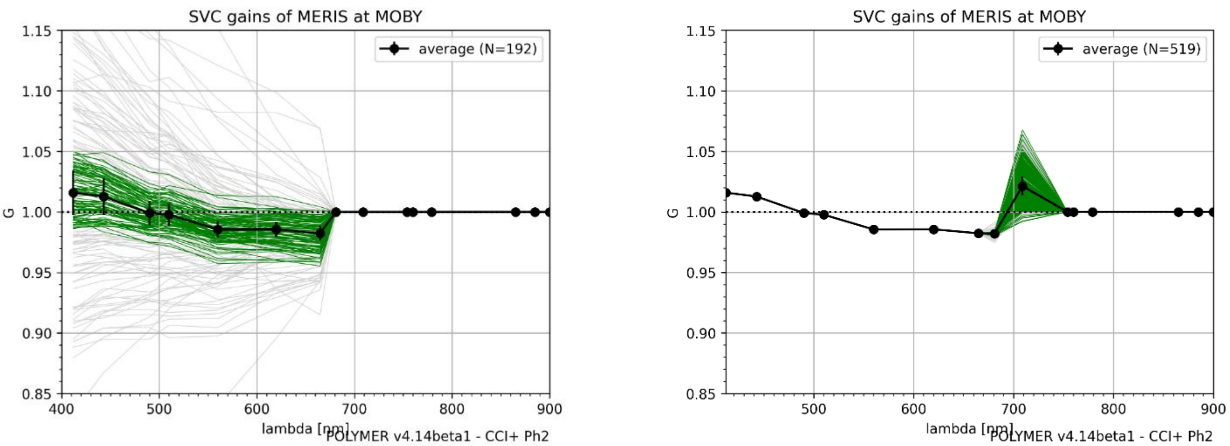

Figure 6. POLYMER vicarious gains derived for MERIS at MOBY as a function of wavelength, left for coupled bands and right for decoupled bands. Solid grey lines represent individual gains, with green overlay when they are within the MSIQR. Black line with dots is the mission mean gain.

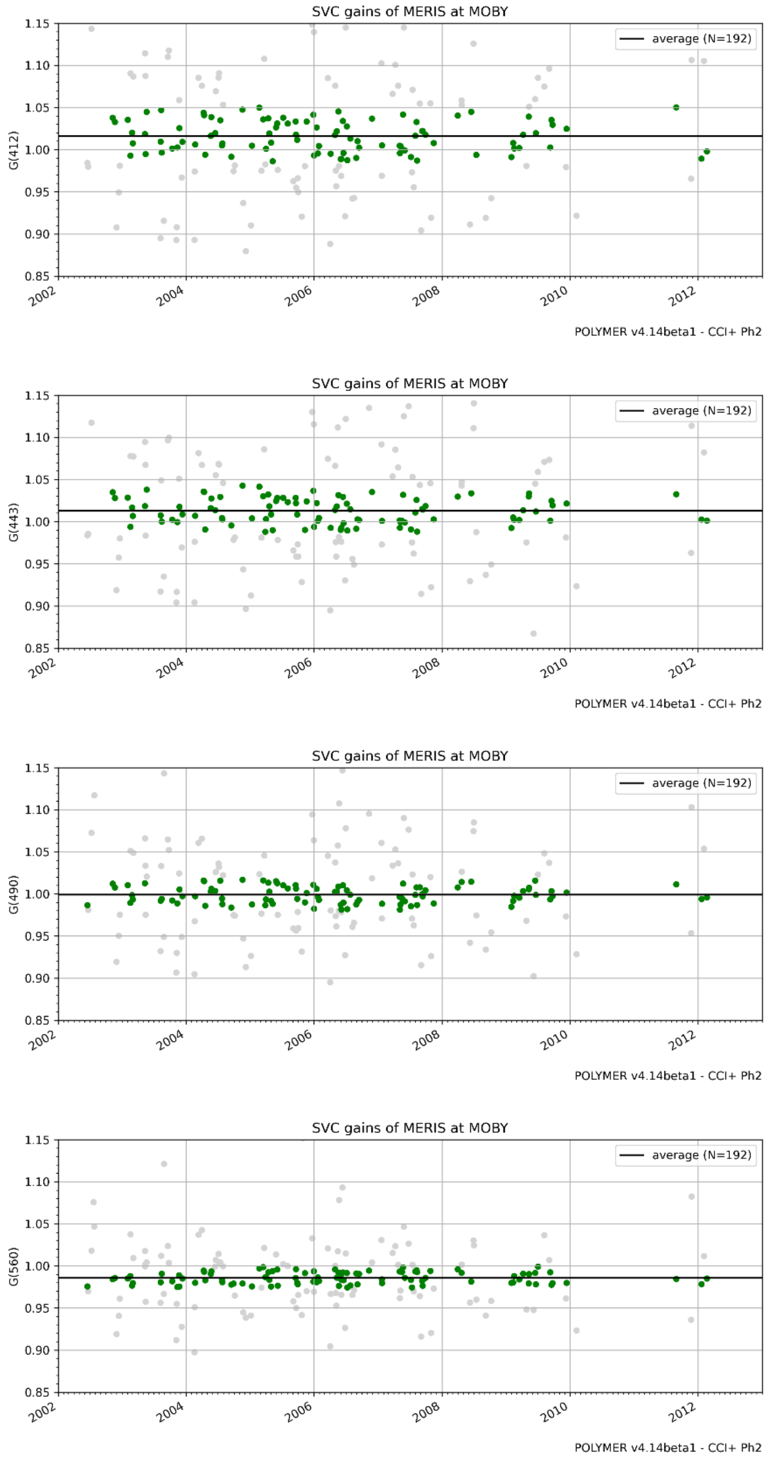

Figure 7. Time-series of POLYMER vicarious gains derived for MERIS at MOBY at 412, 443, 490 and 560 nm (from top to bottom). Circles represent all individual gains, with dark fill when they are within the MSIQR. Black line is the mission average gain.

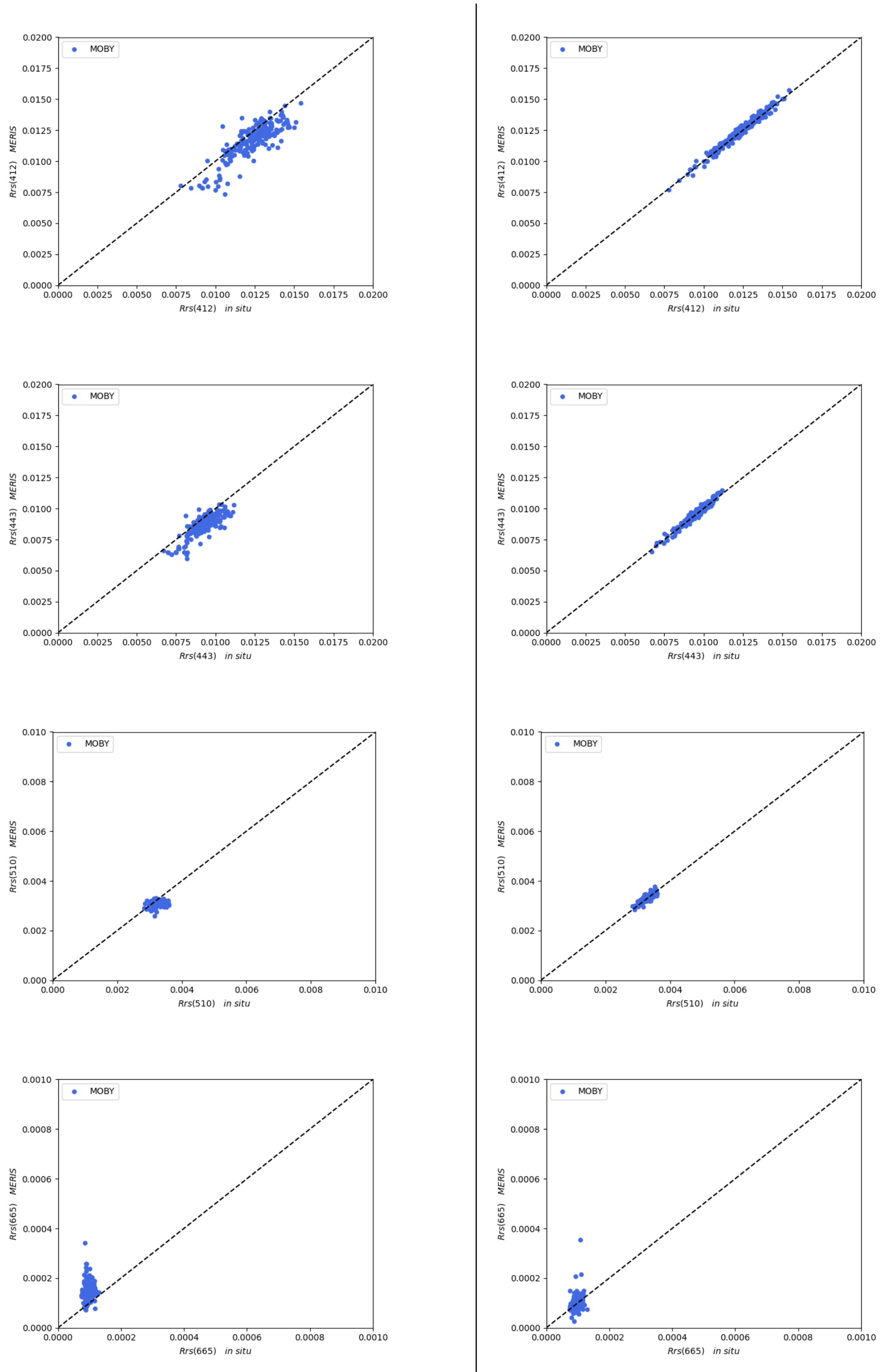

Figure 8. Validation of MERIS ρ_w at MOBY before (left) and after (right) applying pixel-by-pixel gains.

MODIS gains

The choice of bands for SVC of MODIS is given in Table 4. Three bands are fixed in the NIR and six bands are handled in the coupled SVC.

Table 4. POLYMER & SVC band set configuration for MODIS.

Sensor bands (Level-2 output)	Used in AC	Fixed for SVC	Used for SVC – coupled step	Used for SVC – decoupled step
412	✓		✓	
443	✓		✓	
488	✓		✓	
531	✓		✓	
547	✓		✓	
667	✓		✓	
678	✓	✓		
748	✓	✓		
869	✓	✓		

MODIS average gains are provided in Table 5 and spectral shapes of all individual gains are displayed on Figure 9. Time-series of individual gains are provided in Figure 10. Validation before and after individual gains is shown in Figure 11 and demonstrates, as for MERIS, relevance of the selected gains per match-ups.

Table 5. Averaged POLYMER vicarious gains derived for MODIS at MOBY. Asterisk stands for fixed gains.

Band	N	$\bar{g}$	σ	RSEM
412	187	0.998032	0.017519	0.00181
443	187	1.002437	0.015165	0.00156
488	187	0.999126	0.01117	0.001153
531	187	0.998477	0.008768	0.000905
547	187	0.997932	0.007633	0.000788
667	187	1.001547	0.001791	0.000184
678	NA	$1^{(*)}$	NA	NA
748	NA	$1^{(*)}$	NA	NA
869	NA	$1^{(*)}$	NA	NA

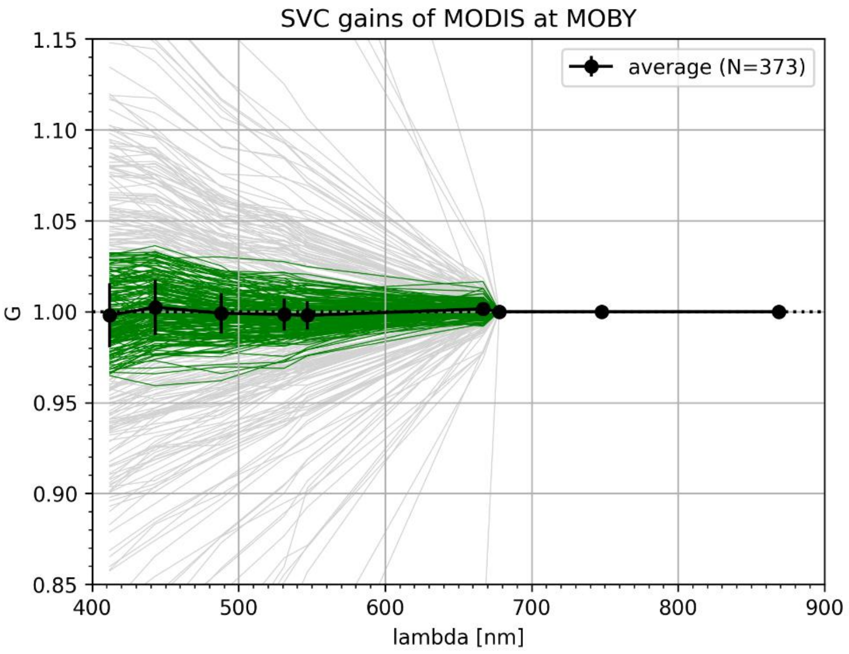

Figure 9. POLYMER vicarious gains derived for MODIS at MOBY as a function of wavelength. Solid grey lines represent individual gains, with green overlay when they are within the MSIQR. Black line with dots is the mission mean gain.

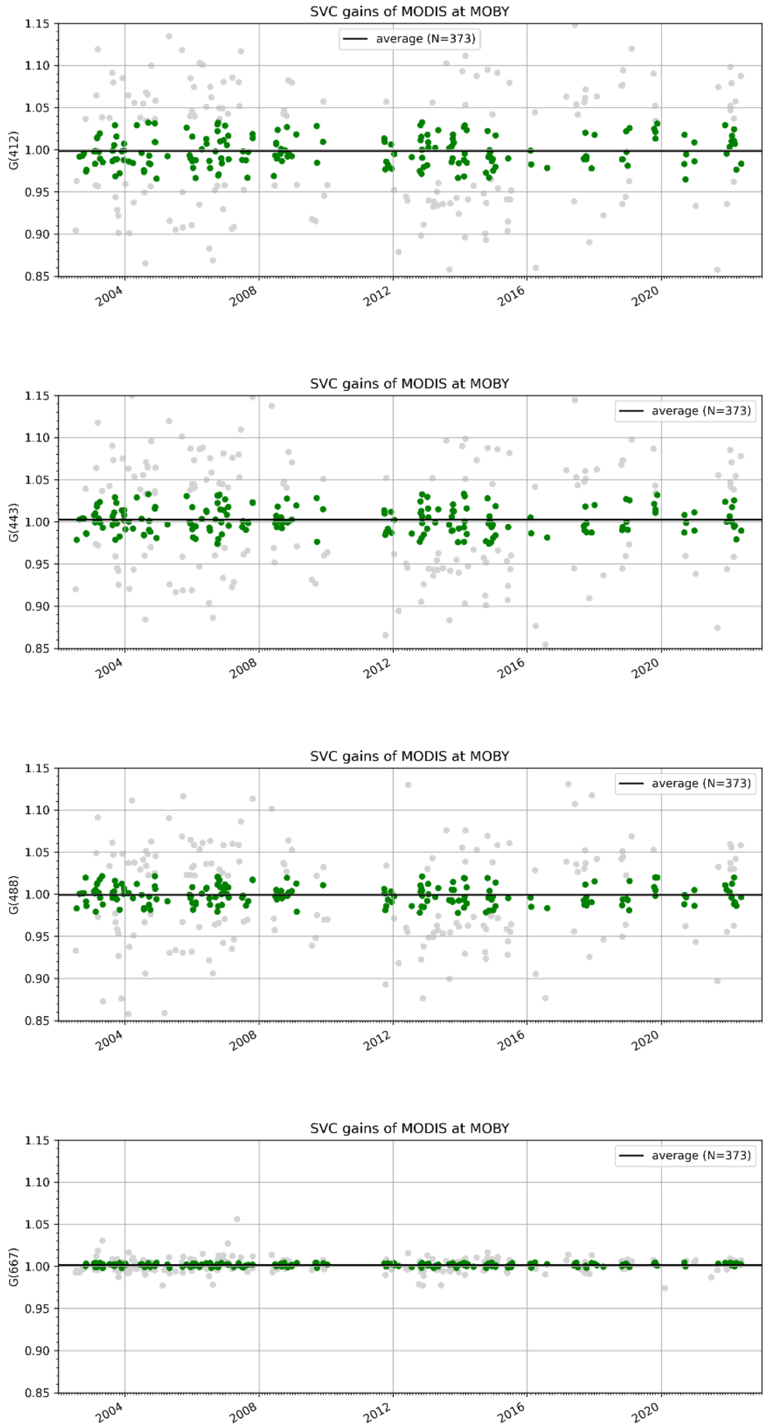

Figure 10. Time-series of POLYMER vicarious gains derived for MODIS at MOBY at 412, 443, 488 and 667 nm (from top to bottom). Circles represent all individual gains, with dark fill when they are within the MSIQR. Black line is the mission average gain.

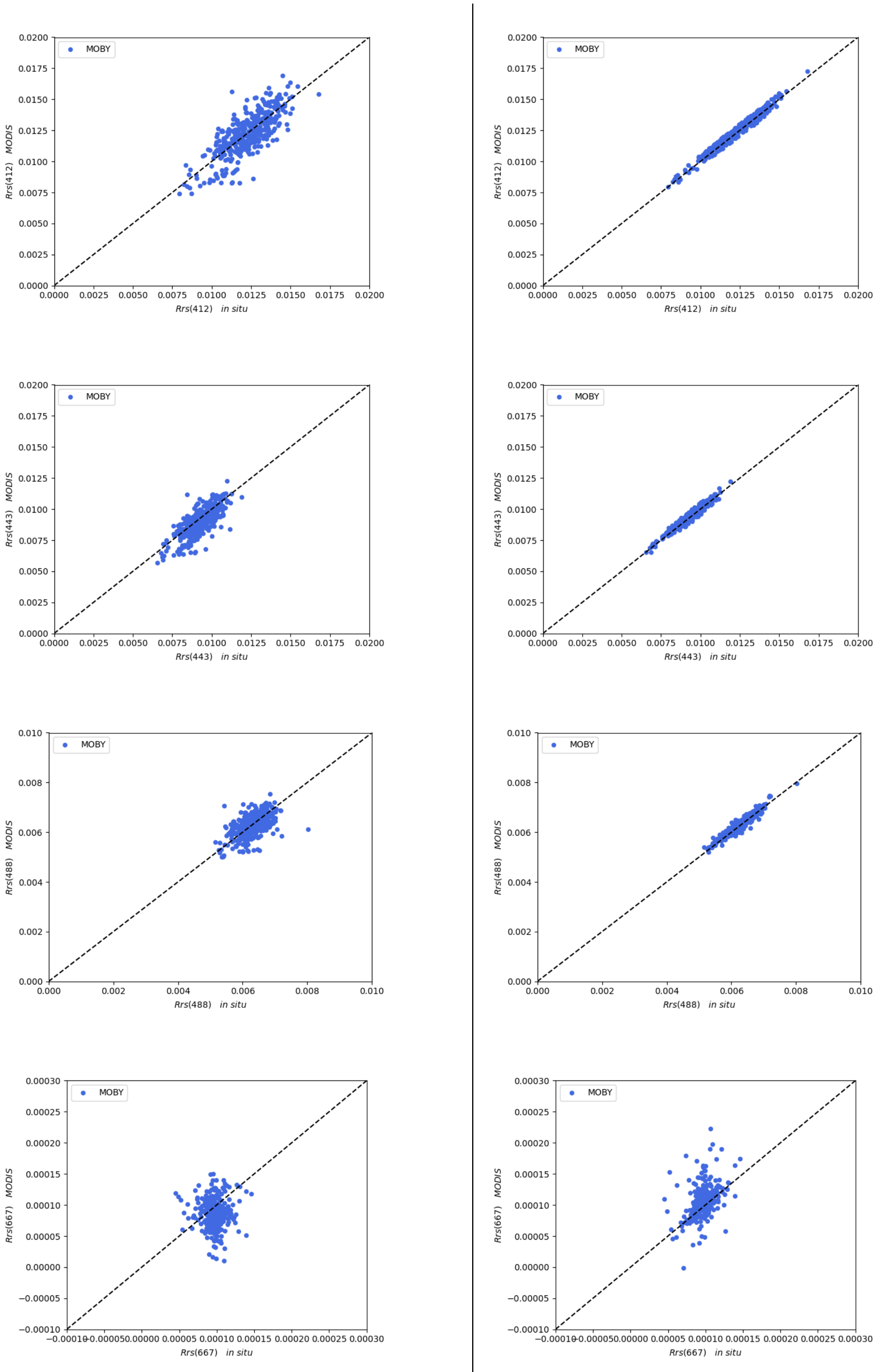

Figure 11. Validation of MODIS ρ_w at MOBY before (left) and after (right) applying pixel-by-pixel gains.

OLCI-A gains

The choice of bands for SVC of OLCI-A is given in Table 6. Three bands are fixed in the NIR, six are handled in the coupled SVC, and five in the decoupled SVC.

Table 6. POLYMER & SVC band set configuration for OLCI-1.

Sensor bands (Level-2 output)	Used in AC	Fixed for SVC	Used for SVC – coupled step	Used for SVC – decoupled step
400				✓
412				✓
443	✓		✓	
490	✓		✓	
510	✓		✓	
560	✓		✓	
620	✓		✓	
665	✓		✓	
681				✓
709				✓
754	✓	✓		
789	✓	✓		
865	✓	✓		
1020				✓

OLCI-A average gains are provided in Table 7 and spectral shapes of all individual gains are displayed on Figure 12 (for the decoupled and coupled steps). Time-series of individual gains are provided in Figure 13. Validation before and after individual gains is shown in Figure 14; individual gains yield a significant improvement, yet we observe a very slight overestimate of marine reflectance for coupled bands, contrary to MERIS or MODIS. For decoupled bands (like 412 nm on Figure 14), the match is perfect, as we expect for standard AC.

Table 7. Averaged POLYMER vicarious gains derived for OLCI-A at MOBY. Asterisk stands for fixed gains.

Band	N	$\bar{g}$	σ	RSEM
400	92	0.992768	0.005099	0.000513
412	92	0.987377	0.005093	0.000515
443	65	0.995437	0.001246	0.000149
490	65	0.986123	0.002279	0.000275
510	65	0.98803	0.002139	0.000257
560	65	0.993077	0.002314	0.000277
620	65	0.997434	0.003598	0.000428
665	65	0.994448	0.003713	0.000444
681	92	0.990531	0.000694	0.00007
709	92	1.026283	0.004805	0.000468

754	NA	1(*)	NA	NA
779	NA	1(*)	NA	NA
865	NA	1(*)	NA	NA
1020	92	0.923525	0.019072	0.002062

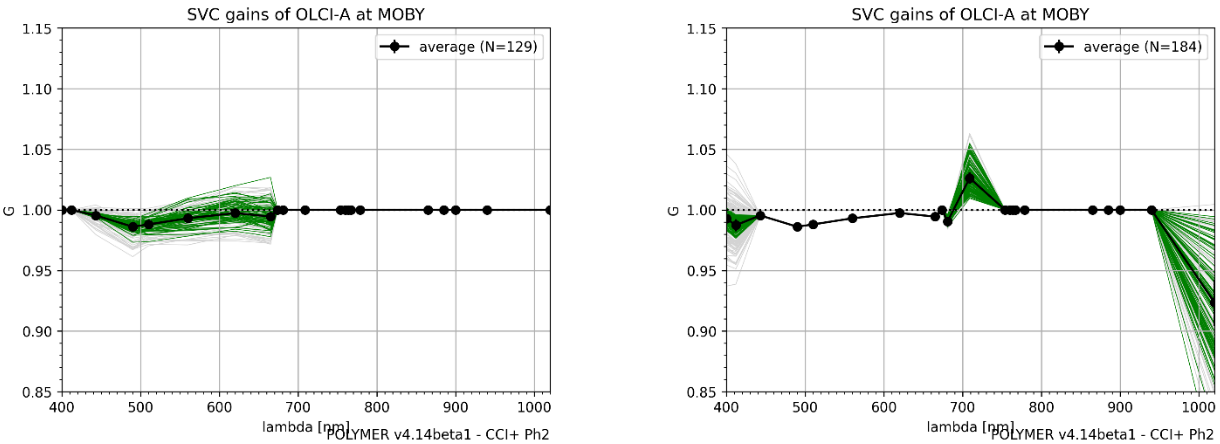

Figure 12. POLYMER vicarious gains derived for OLCI-A at MOBY as a function of wavelength, left for coupled bands and right for decoupled bands. Solid grey lines represent individual gains, with green overlay when they are within the MSIQR. Black line with dots is the mission mean gain.

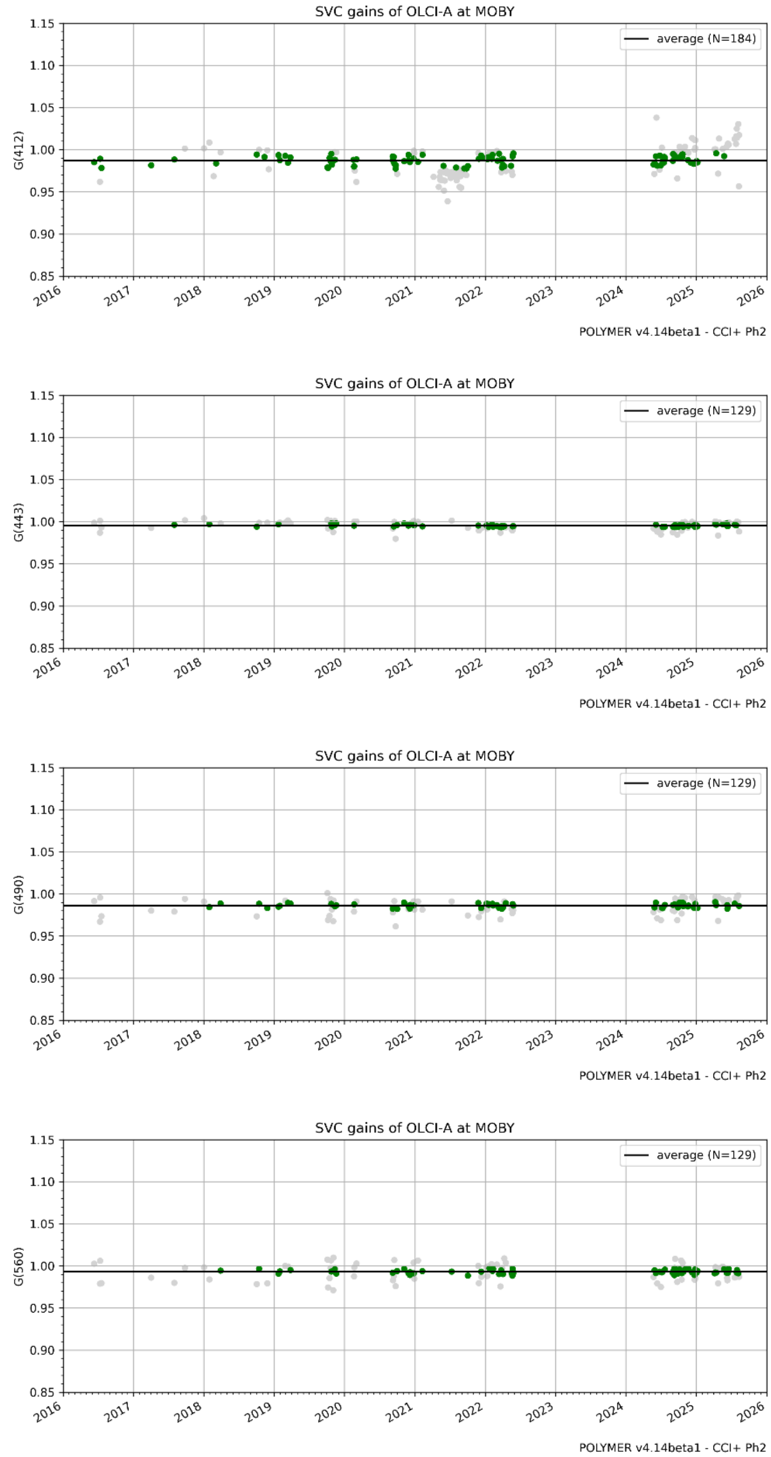

Figure 13. Time-series of POLYMER vicarious gains derived for OLCI-A at MOBY at 412, 443, 490 and 560 nm (from top to bottom). Circles represent all individual gains, with dark fill when they are within the MSIQR. Black line is the mission average gain.

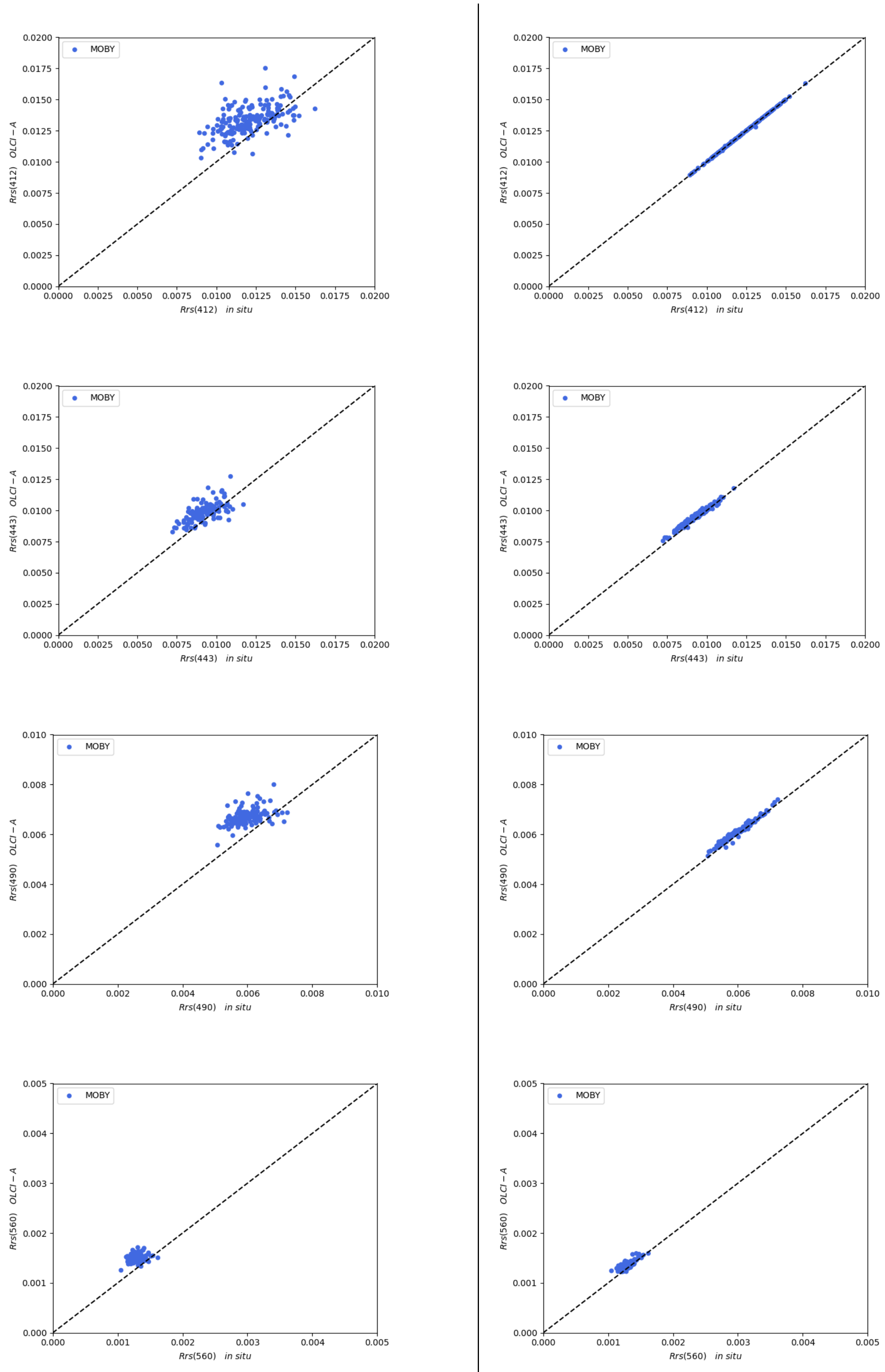

Figure 14. Validation of OLCI-A ρ_w at MOBY before (left) and after (right) applying pixel-by-pixel gains.

OLCI-B gains

The choice of bands for SVC of OLCI-B is similar to OLCI- A and reproduced in Table 8. Three bands are fixed in the NIR, six are handled in the coupled SVC, and five in the decoupled SVC.

Table 8. POLYMER & SVC band set configuration for OLCI-B.

Sensor bands (Level-2 output)	Used in AC	Fixed for SVC	Used for SVC – coupled step	Used for SVC – decoupled step
400				✓
412				✓
443	✓		✓	
490	✓		✓	
510	✓		✓	
560	✓		✓	
620	✓		✓	
665	✓		✓	
681				✓
709				✓
754	✓	✓		
789	✓	✓		
865	✓	✓		
1020				✓

OLCI-B average gains are provided in Table 9 and spectral shapes of all individual gains are displayed on Figure 15 (for the decoupled and coupled steps). The SVC gains are very similar to those of OLCI-A, despite the known discrepancy between the sensors at TOA (about 2% overbrightness for OLCI-A); this shows that POLYMER gains strongly relate to the AC itself and its embedded modelling (marine and atmospheric), contrary to standard AC which is strongly dependent on the TOA radiometry and calibration. Time-series of individual gains are provided in Figure 16. Validation before and after individual gains is shown in Figure 17, and present performance similar to that of OLCI-A: perfect match for decoupled band, and nearly perfect impact for coupled bands (reflectance slightly overestimated).

Table 9. Averaged POLYMER vicarious gains derived for OLCI-B at MOBY. Asterisk stands for fixed gains.

Band	N	$\bar{g}$	σ	RSEM
400	104	0.995179	0.004797	0.000391
412	104	0.988385	0.004523	0.000371
443	80	0.995679	0.001396	0.00013
490	80	0.986421	0.002505	0.000235
510	80	0.987526	0.002215	0.000208
560	80	0.990882	0.003007	0.000281
620	80	0.997389	0.004101	0.000381
665	80	0.994899	0.004846	0.000451
681	104	0.992028	0.000732	0.00006
709	104	1.026224	0.004422	0.00035

754	NA	1(*)	NA	NA
779	NA	1(*)	NA	NA
865	NA	1(*)	NA	NA
1020	104	0.933837	0.018697	0.001625

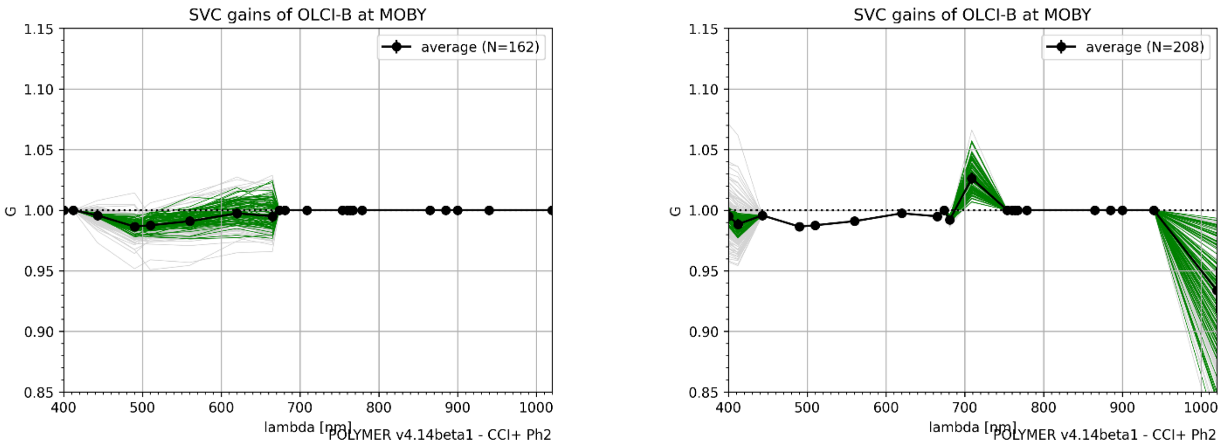

Figure 15. POLYMER vicarious gains derived for OLCI-B at MOBY as a function of wavelength, left for coupled bands and right for decoupled bands. Solid grey lines represent individual gains, with green overlay when they are within the MSIQR. Black line with dots is the mission mean gain.

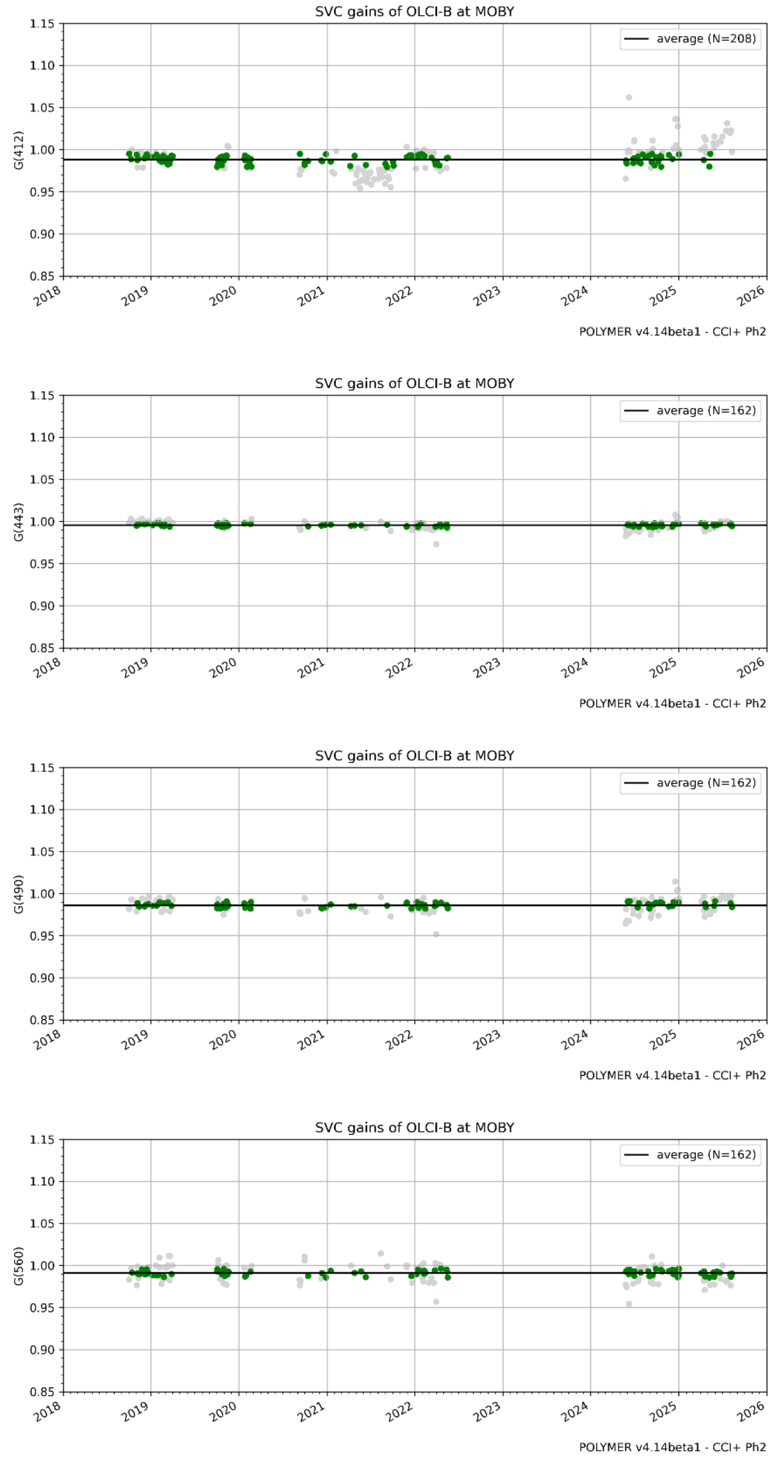

Figure 16. Time-series of POLYMER vicarious gains derived for OLCI-B at MOBY at 412, 443, 490 and 560 nm (from top to bottom). Circles represent all individual gains, with dark fill when they are within the MSIQR. Black line is the mission average gain.

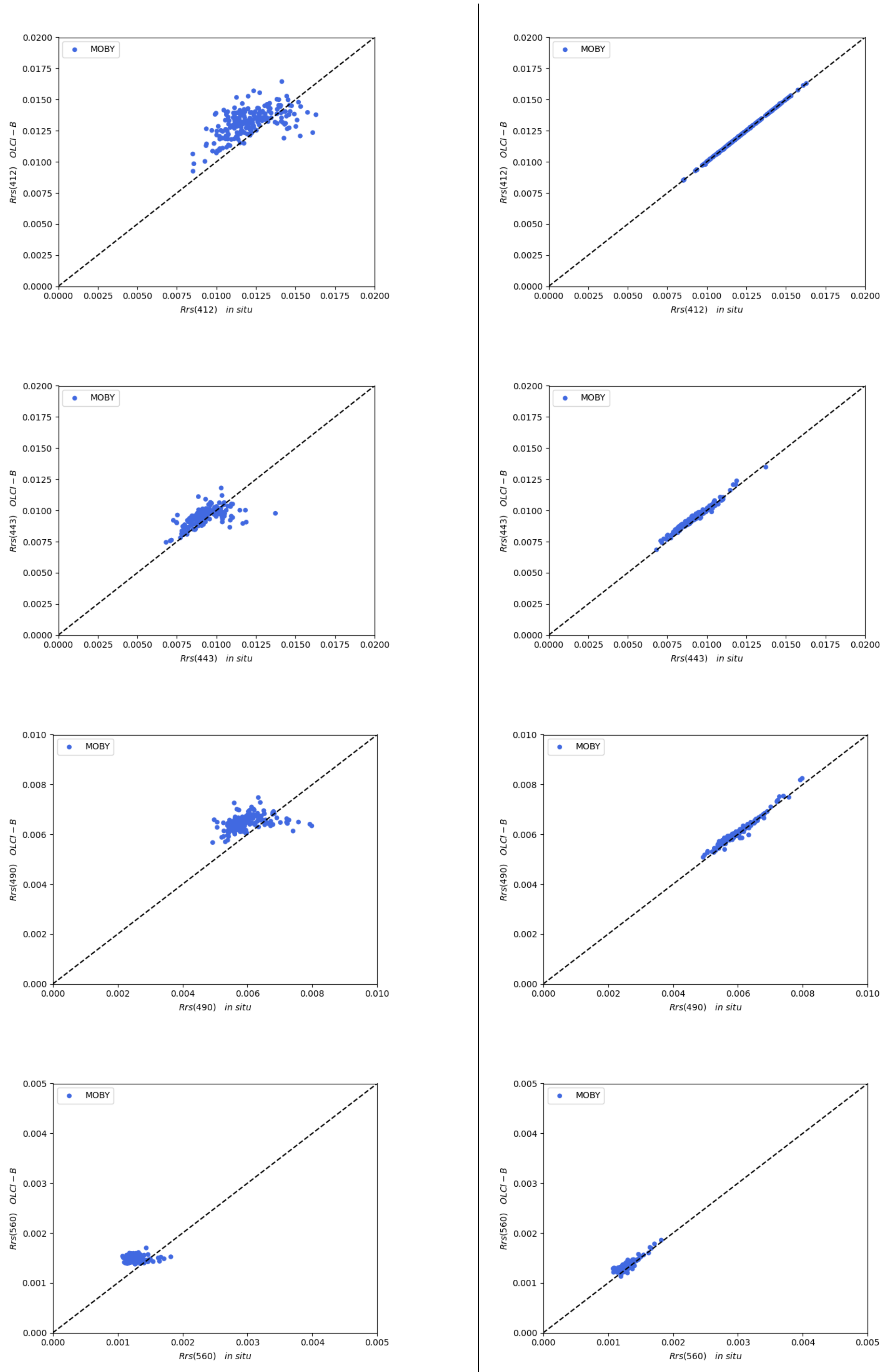

Figure 17. Validation of OLCI-B ρ_w at MOBY before (left) and after (right) applying pixel-by-pixel gains.

VIIRSN gains

The choice of bands for SVC of VIIRSN is given in Table 10. Three bands are fixed in the NIR, three are handled in the coupled SVC, and one in the decoupled SVC.

Table 10. POLYMER & SVC band set configuration for VIIRSJ1.

Sensor bands (Level-2 output)	Used in AC	Fixed for SVC	Used for SVC – coupled step	Used for SVC – decoupled step
410				✓
443	✓		✓	
486	✓		✓	
551	✓		✓	
671	✓	✓		
745	✓	✓		
862	✓	✓		

VIIRSN average gains are provided in Table 11 and spectral shapes of all individual gains are displayed on Figure 18 (for the decoupled and coupled steps). Time-series of individual gains are provided in Figure 19. Validation before and after individual gains is shown in Figure 20; we retrieve an excellent performance for the selected gains, like MERIS and MODIS.

Table 11. Averaged POLYMER vicarious gains derived for VIIRSN at MOBY. Asterisk stands for fixed gains.

Band	N	$\bar{g}$	σ	RSEM
410	357	0.985082	0.004631	0.000289
443	160	0.968889	0.005469	0.000518
486	160	0.99844	0.003769	0.000347
551	160	0.991118	0.001805	0.000167
671	NA	1(*)	NA	NA
745	NA	1(*)	NA	NA
862	NA	1(*)	NA	NA

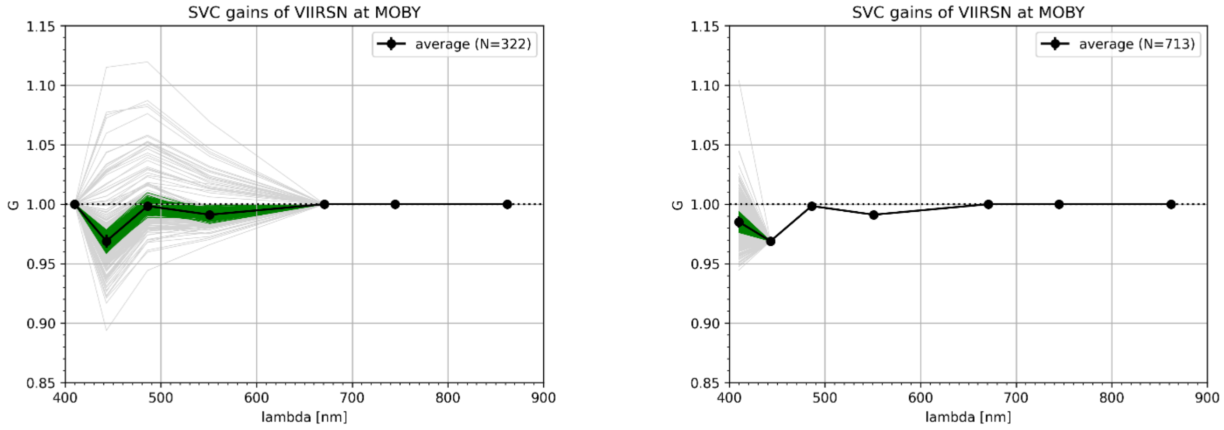

Figure 18. POLYMER vicarious gains derived for VIIRSN at MOBY as a function of wavelength, left for coupled bands and right for decoupled bands. Solid grey lines represent individual gains, with green overlay when they are within the MSIQR. Black line with dots is the mission mean gain.

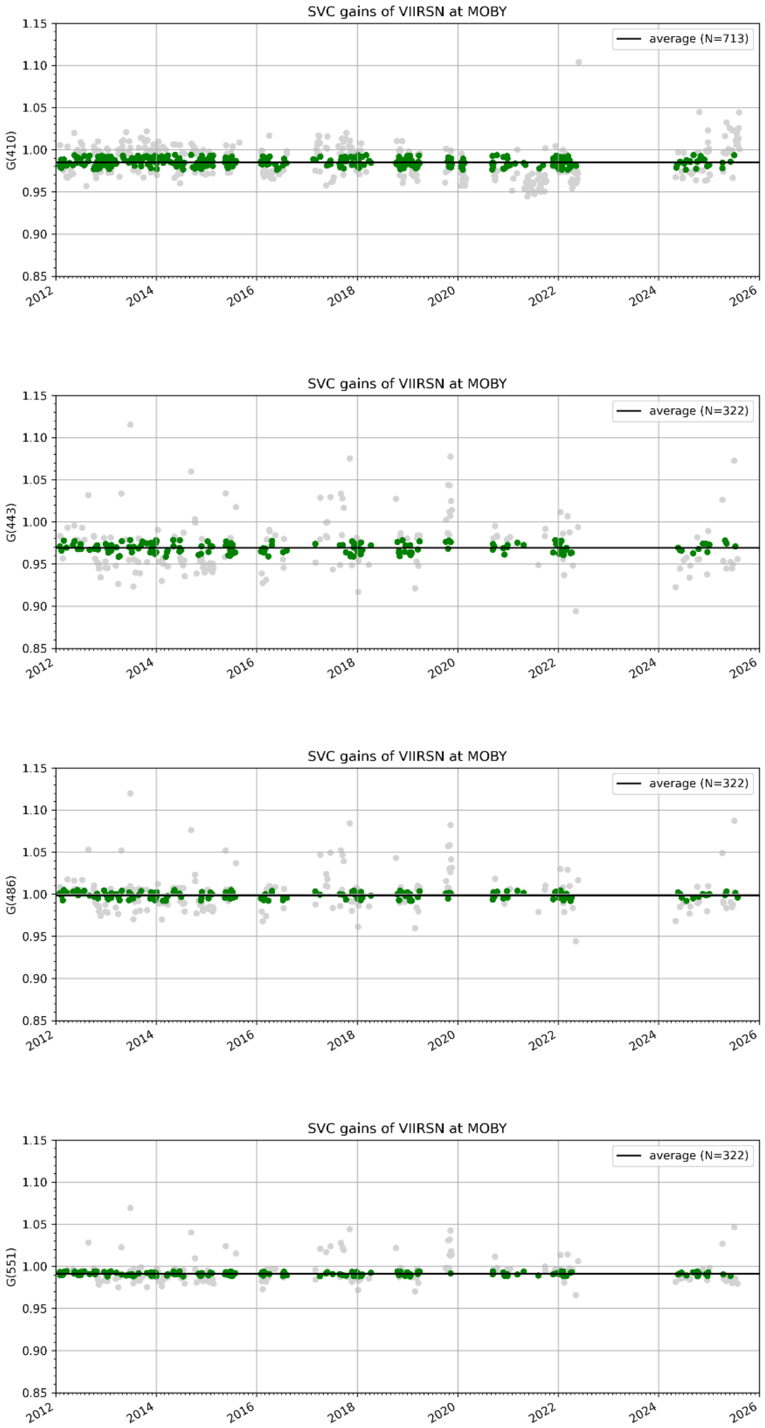

Figure 19. Time-series of POLYMER vicarious gains derived for VIIRSN at MOBY at 410, 443, 486 and 551 nm (from top to bottom). Circles represent all individual gains, with dark fill when they are within the MSIQR. Black line is the mission average gain.

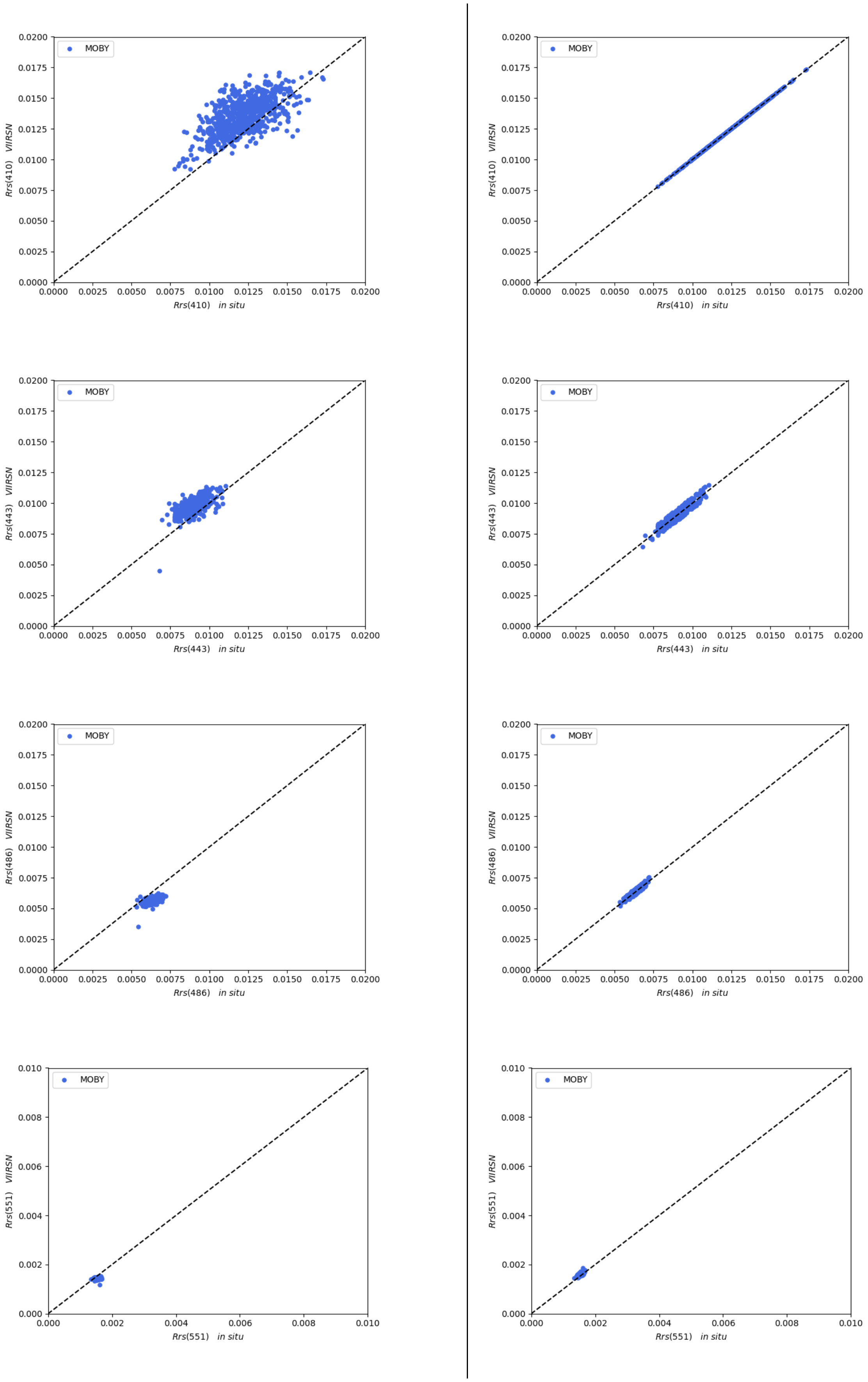

Figure 20. Validation of VIIRSN ρ_w at MOBY before (left) and after (right) applying pixel-by-pixel gains.

VIIRSJ1 gains

The choice of bands for SVC of VIIRSJ1 is given in Table 12. Three bands are fixed in the NIR, three are handled in the coupled SVC, and one in the decoupled SVC.

Table 12. POLYMER & SVC band set configuration for VIIRSJ1.

Sensor bands (Level-2 output)	Used in AC	Fixed for SVC	Used for SVC – coupled step	Used for SVC – decoupled step
412				✓
445	✓		✓	
489	✓		✓	
556	✓		✓	
667	✓	✓		
746	✓	✓		
868	✓	✓		

VIIRSJ1 average gains are provided in Table 13 and spectral shapes of all individual gains are displayed on Figure 21 (for the decoupled and coupled steps). Time-series of individual gains are provided in Figure 22. Validation before and after individual gains is shown in Figure 23 and demonstrates relevance of the selected gains.

Table 13. Averaged POLYMER vicarious gains derived for VIIRSJ1 at MOBY. Asterisk stands for fixed gains.

Band	N	$\bar{g}$	σ	RSEM
411	152	0.99941	0.005565	0.000374
445	50	1.001023	0.005896	0.00069
489	50	1.005986	0.004709	0.000548
556	50	0.996256	0.003009	0.000354
667	NA	1(*)	NA	NA
746	NA	1(*)	NA	NA
868	NA	1(*)	NA	NA

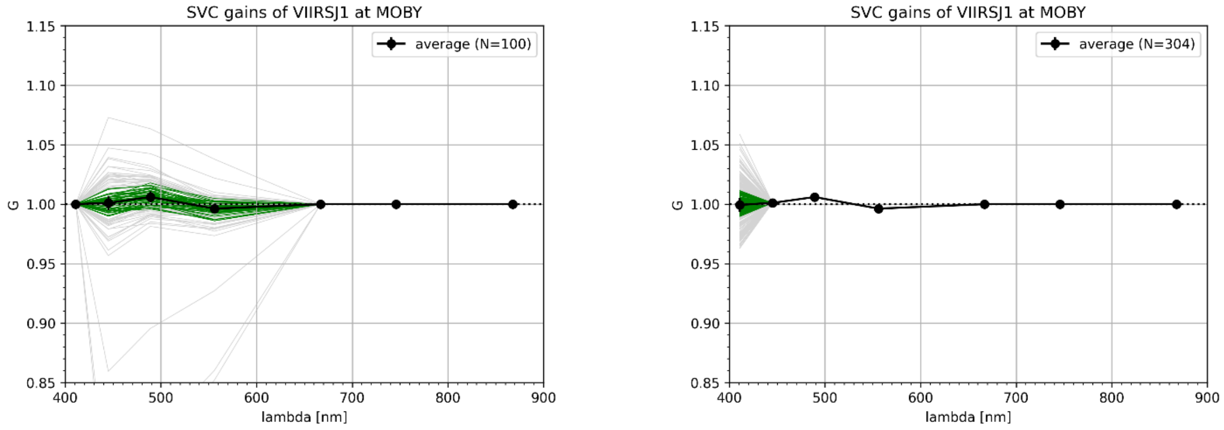

Figure 21. POLYMER vicarious gains derived for VIIRSJ1 at MOBY as a function of wavelength, left for coupled bands and right for decoupled bands. Solid grey lines represent individual gains, with green overlay when they are within the MSIQR. Black line with dots is the mission mean gain.

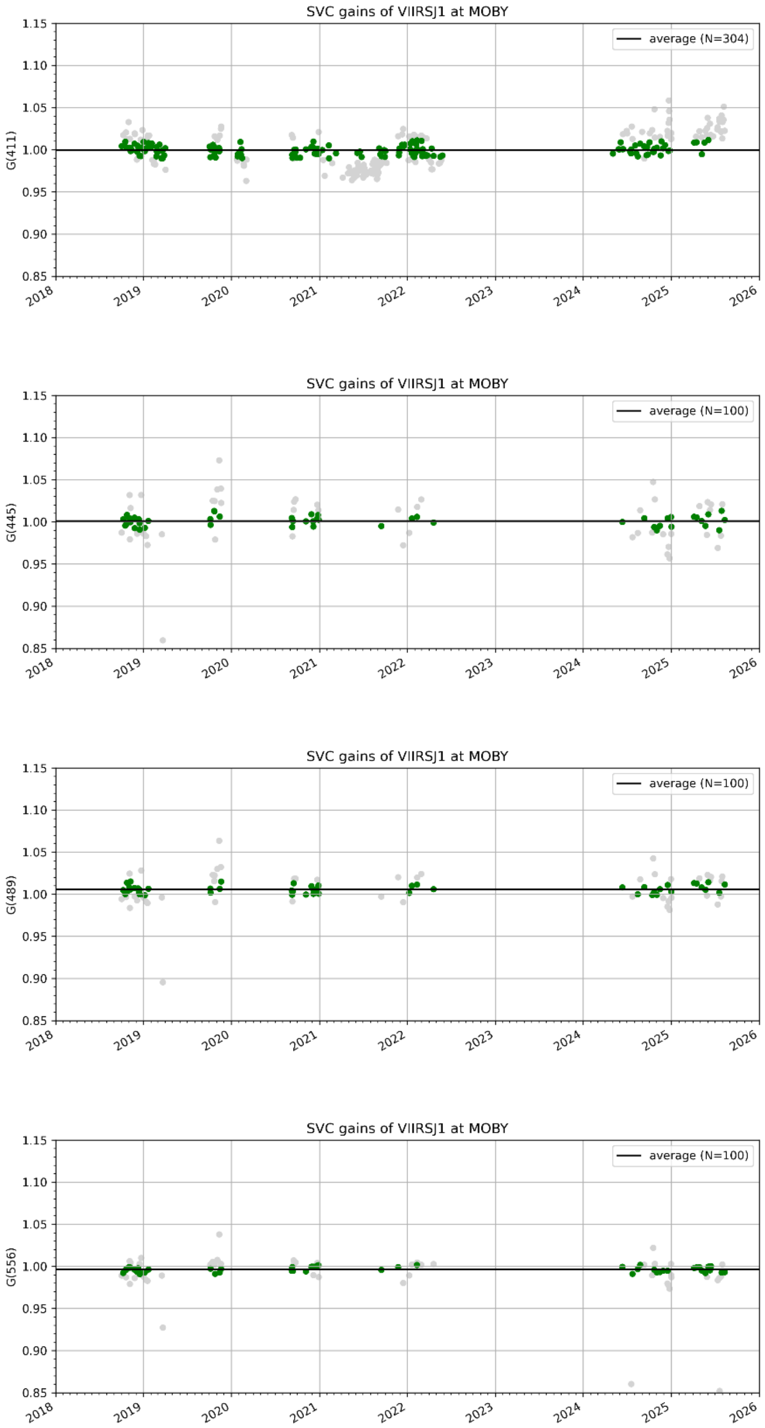

Figure 22. Time-series of POLYMER vicarious gains derived for VIIRSJ1 at MOBY at 411, 445, 489 and 556 nm (from top to bottom). Circles represent all individual gains, with dark fill when they are within the MSIQR. Black line is the mission average gain.

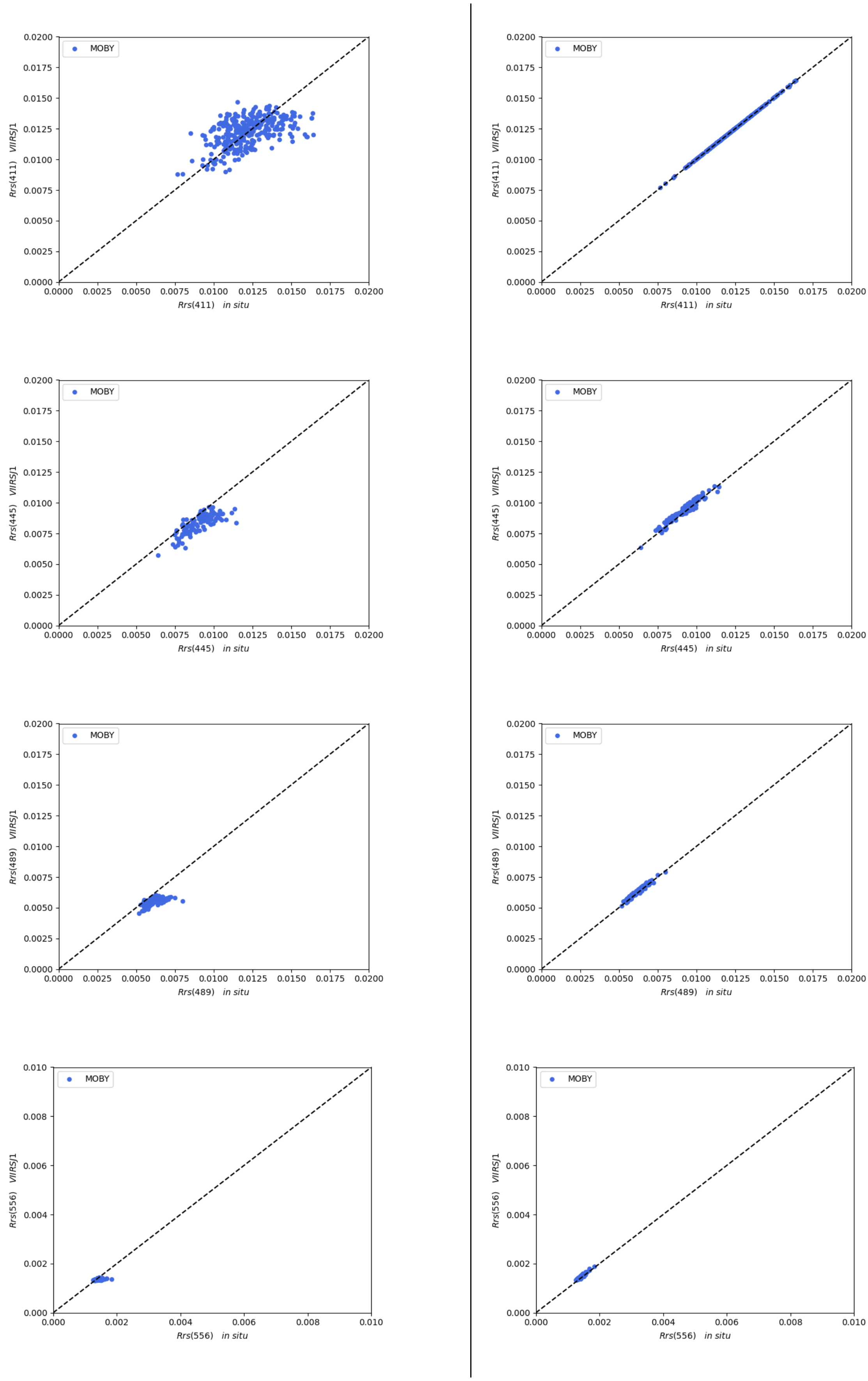

Figure 23. Validation of VIIRSJ1 ρ_w at MOBY before (left) and after (right) applying pixel-by-pixel gains.

5. Discussion and conclusion

Overall analysis of POLYMER average gains

POLYMER average gains are generally small, less than 2% or even less than 1%. This shows the robustness of POLYMER inversion to the instrumental calibration, further discussed hereafter. Typically, OLCI-A and OLCI-B gains are very similar, while it is known that the former is about 2% brighter at TOA than the latter. Hence, these gains essentially adjust the marine-atmosphere coupled model embedded in POLYMER. A different situation occurs at bands 709 nm for MERIS and OLCI and 1020 nm for OLCI, which are not used by POLYMER in the aerosol detection (hence their gains come from the decoupled SVC):

- Band 1020 nm is indeed known to be far too bright at Level-1b, and a correction of about -8% is consistent with the OLCI standard AC (Mazeran and Ruescas, 2020).
- Band 709 nm is impacted by water vapour, which is not handled in current POLYMER code. Hence the gain of more than +2% for MERIS, OLCI-A and OLCI-B adjust for this lack of correction.

VIIRSN also presents a significant correction of more than +3% at 443 nm, which was already observed in previous OC-CCI phase. This relates to the sensor and not the AC, since VIIRSJ1 with very similar bands configuration does not show such pattern.

MODIS, OLCI and VIIRS average gains have generally a rather flat spectral shape (expect for the few bands discussed above). Only MERIS gains present a clear spectral slope (correction decreases from blue to red). Standard SVC of MERIS 4th reprocessing data also showed a slope, but in the opposite direction (correction increasing from blue to red). This demonstrates again the major role played by the coupled ocean-atmosphere model embedded in the AC.

Finally, time-series of individual gains present a very robust stability, confirmed after screening by RSEM values well below the targeted 0.5% of Zibordi et al. (2015), for all bands and sensors.

Relevance and limits of the optimal gains

All scatter plots after application of individual gains (*Figure 8*, *Figure 11*, *Figure 14*, *Figure 17*, *Figure 20*, *Figure 23*) shows a very good match by definition of the data screening: match-ups are removed if after calibration the difference with in situ reflectance is larger than $5x10^{-4}$. This is justified in order to keep only the most meaningful individual gains, before the statistical screening and averaging on the gain's distribution (MSIQR average). However, a number of points diverge (not shown on the graph and not kept in the averaging), which illustrates the challenge of computing gains for spectrally coupled AC. On the contrary, the match is perfect for decoupled bands, as expected (e.g. band 412 for OLCI in *Figure 14* and *Figure 17*, band 410 for VIIRS on *Figure 20* and *Figure 23*); here we retrieve the behaviour of standard AC.

Furthermore, the effect of average gains may also be limited, compared to standard AC. Indeed, in the decoupled case, the average gains allow to remove systematic bias at BOA, strictly at the calibration site, and possibly at other sites when the initial discrepancy comes from a systematic effect in instrumental calibration. The limitations are well-known for the standard SVC (Franz et al., 2007): "*As the observation conditions deviate from the nominal conditions and geometries of the vicarious calibration targets, the ability of the vicarious calibration to compensate for algorithm error will be diminished. For example, in some coastal and inland waters, the typical aerosol may not be well represented by the operational aerosol model suite or model selection process. Similarly, these more complex cases may trigger components of the atmospheric correction algorithm that are rarely exercised over open oceans, such as the correction for nonzero Lw(NIR) in turbid or eutrophic waters*". Very interestingly, the limits of the standard SVC are reached when non-linear effects come into play - typically the iterative correction for turbid water involving a marine model (Bailey et al. 2010) - and logically they apply to the present case. O'Kane et al. (2024) have also shown the deleterious effect of standard OLCI SVC gains when applied to the Case-2 Regional Coast Colour (C2RCC) neural network (because no SVC methodology exist for this algorithm). They conclude to investigate site-specific gains, in their case over the Baltic Sea, what is however currently out of scope for the OC-CCI at global level. More pragmatically, they simply recommend comparing the performance with and without SVC before any implementation at a larger scale.

Hence, we analyse here the impact of OLCI-A average SVC gains, first at the MarONet site (off Perth, Australia) characterized by clear waters, yet not as oligotrophic as over Hawaii. With unit gains, we observe on *Figure 24* a significant overestimate in the OLCI marine reflectance, at all bands (bias of the order of 10^{-3} in the blue). Applying the gains decreases the signal and reduces the bias to the order of 10^{-4} or even 10^{-5} (*Figure 25*); still, the adjustment is not enough to match more closely the in situ data in the red, at 620 and 665 nm. This is likely due to the necessary trade-off between bands in the optimal SVC, and more precisely because present χ^2_{SVC} cost function is expressed in absolute value; this penalises bands in the red, whose marine reflectance at MOBY is respectively four and seven times smaller than that at 490 and 412 nm.

The same analysis was performed at the AERONET-OC AAOT site, without SVC (*Figure 26*) and with SVC (*Figure 27*). In this case, the water type and atmosphere are very different than those at MOBY (coastal moderately turbid waters and coastal atmosphere). On the scatter plot we first notice two distributions of points: a first set of match-ups relatively well correlated with in situ data, and then a cloud of points largely underestimated. The origin of this second set of points is not further discussed here (possibly an inoperative cloud screening, since we don't apply here the OC-CCI cloud screening algorithm developed by Brockmann et al. 2011). This bimodal distribution makes hard any interpretation of statistics; however, we observe that SVC gains tend to decrease the overestimated marine reflectance in the blue bands. At other bands, the effect of SVC seems minor, and both configurations have satisfying performance (points relatively well distributed around the 1:1 line).

Hence, the application of SVC for OLCI-A is globally beneficial to POLYMER, over different water types. This analysis has to be conducted over more AERONET-OC sites (e.g. absorbing waters in the Baltic Sea) and for all other sensors, as part of the standardized OC-CCI validation activity.

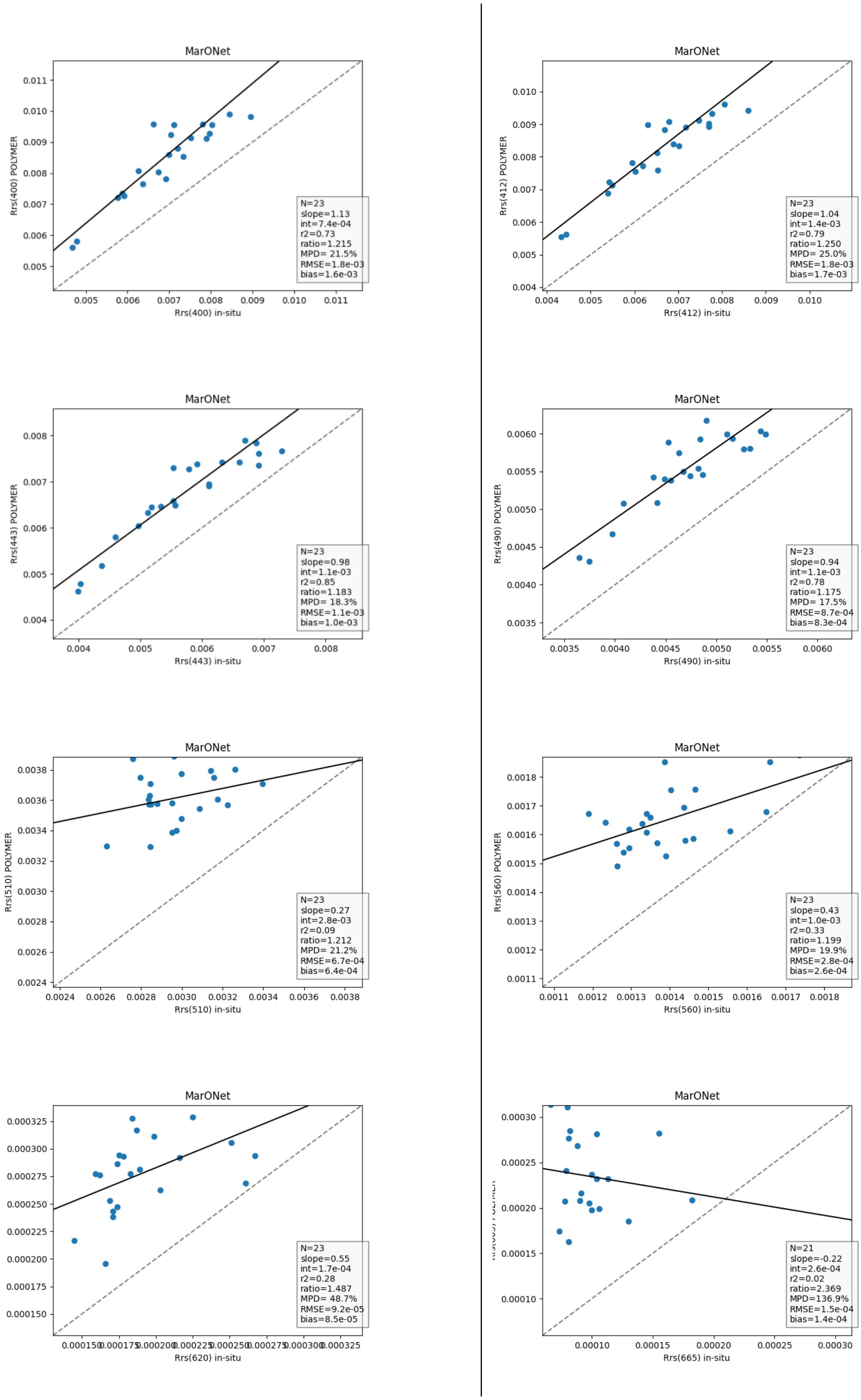

Figure 24. Validation of OLCI-A ρ_w at MaroNet (Perth) before SVC (unit gains)

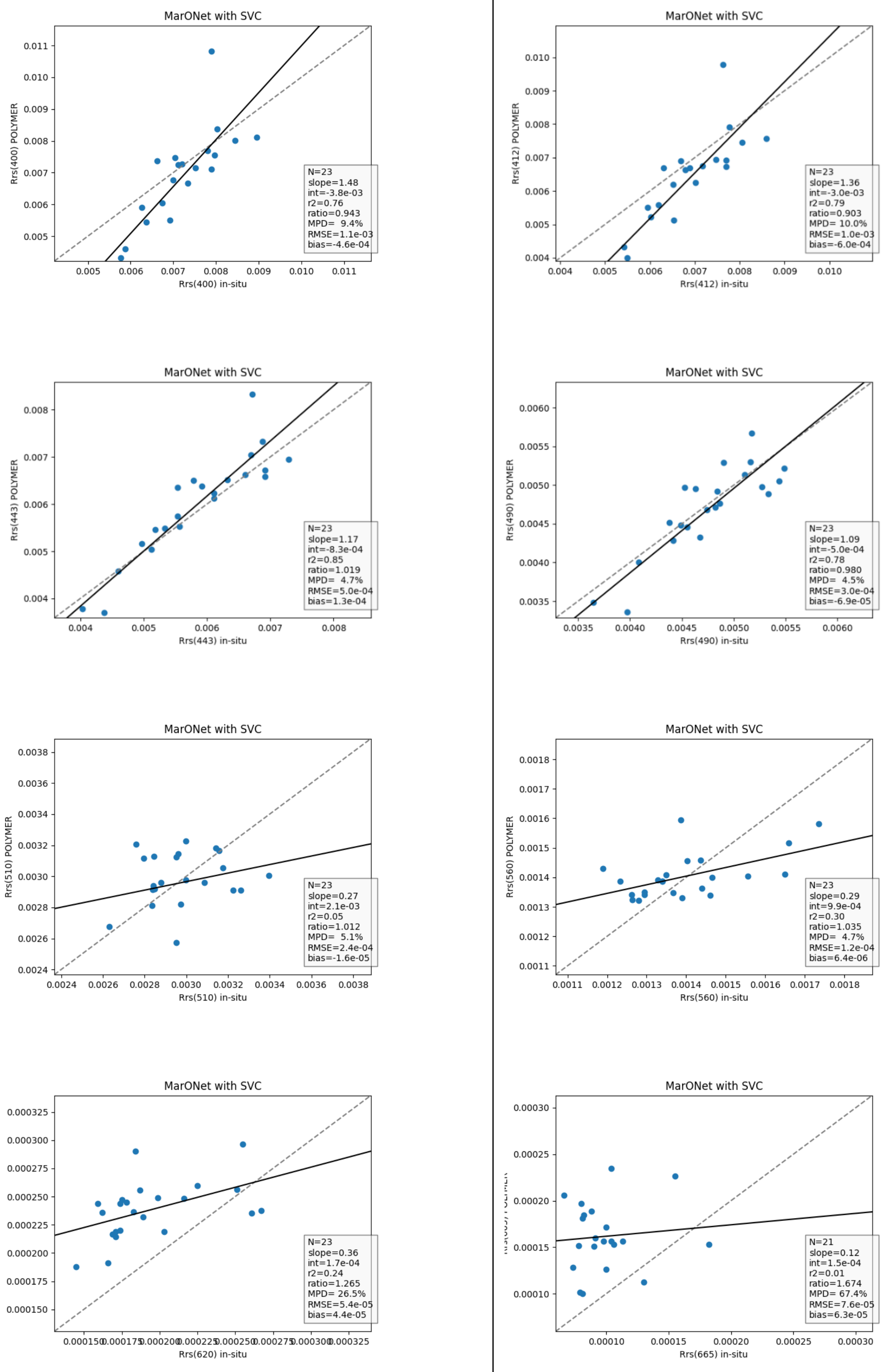

Figure 25. Validation of OLCI-A ρ_w at MaroNet (Perth) after SVC (average gains)

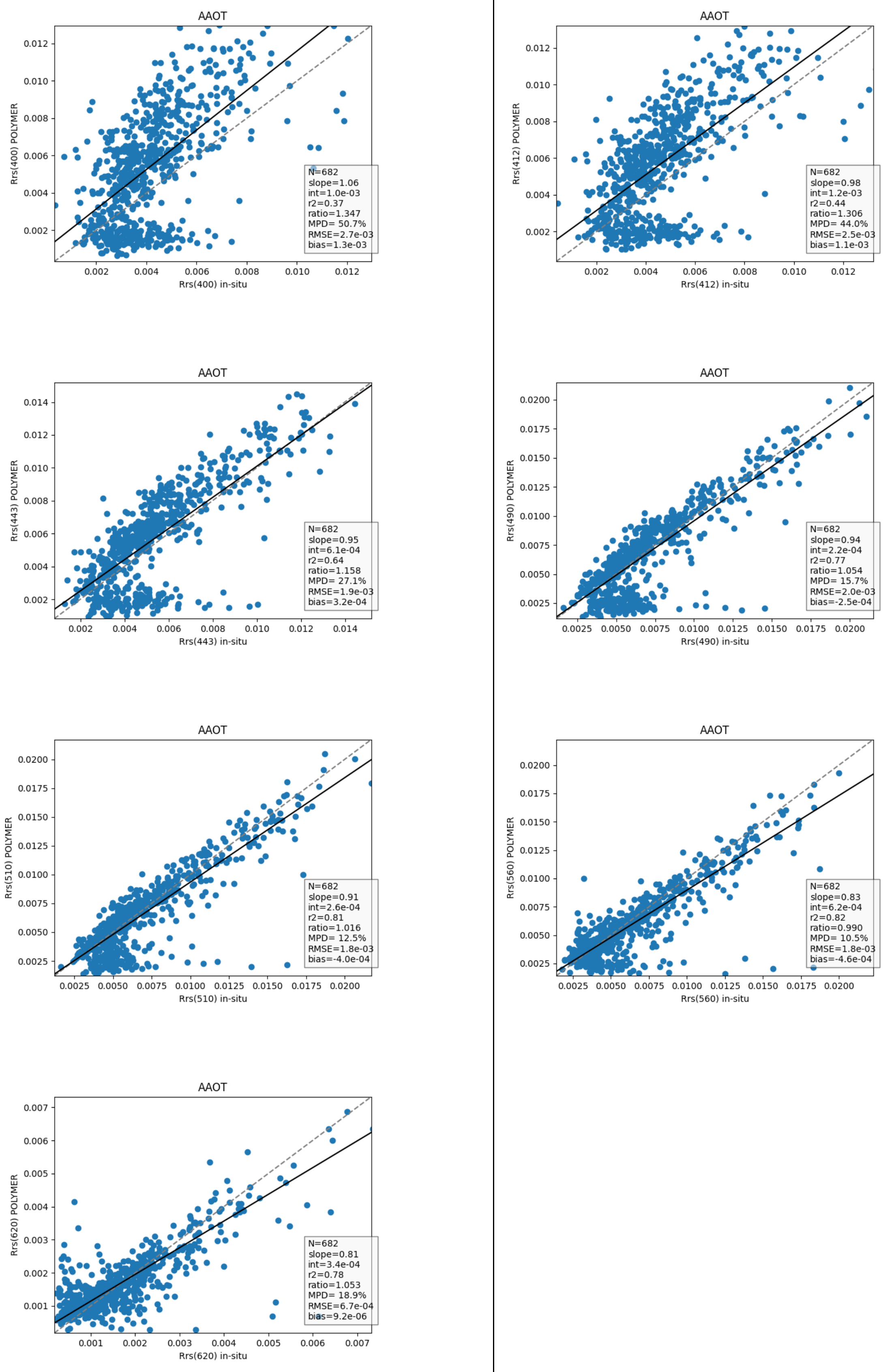

Figure 26. Validation of OLCI-A ρ_w at AAOT before SVC (unit gains)

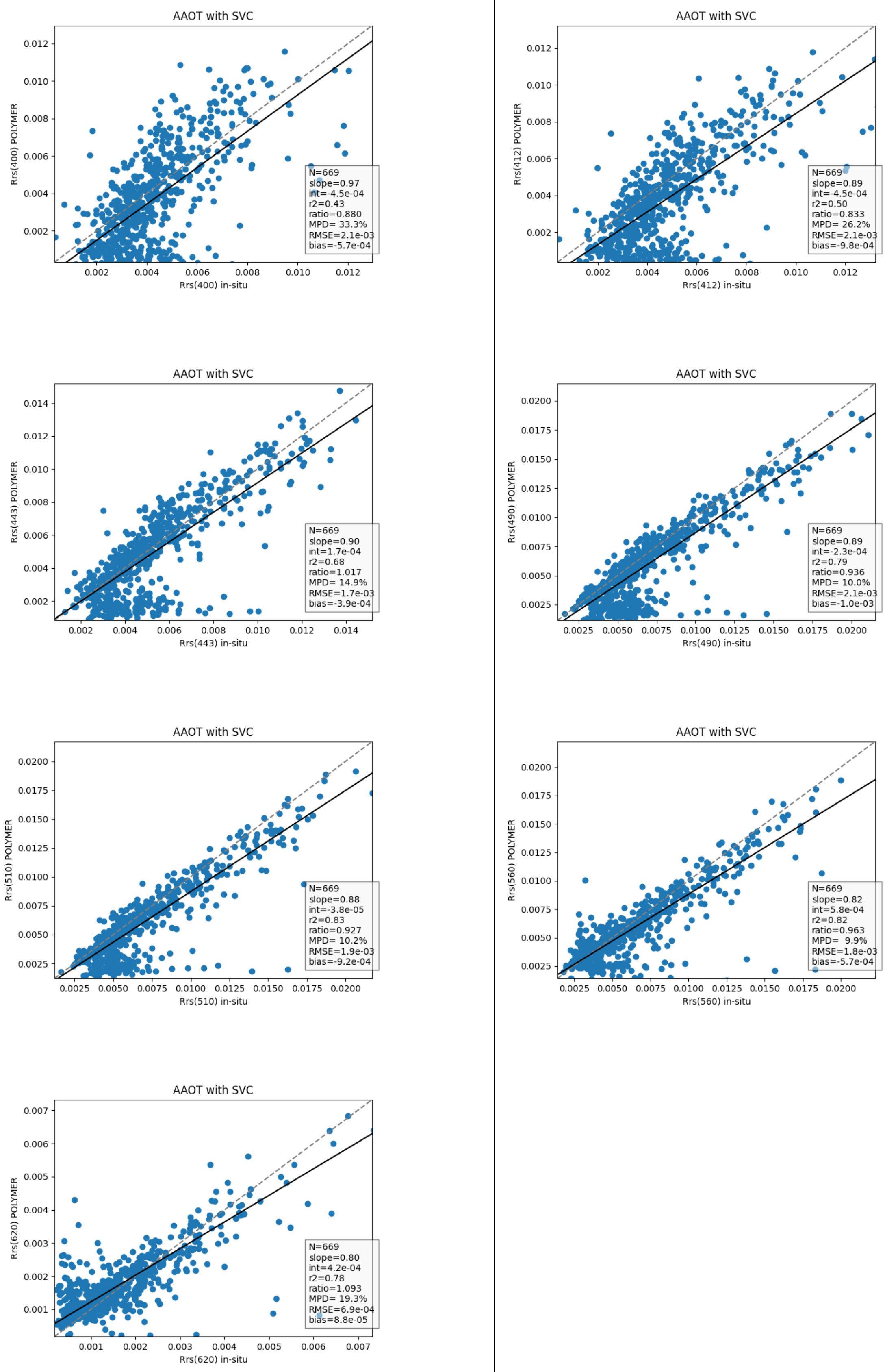

Figure 27. Validation of OLCI-A ρ_w at AAOT after SVC (average gains)

Summary of differences with standard SVC

Major distinctions between the standard and the optimal SVC are listed in Table 14. The prototype algorithms for standard and spectral matching atmospheric corrections are respectively Gordon and Wang (1994) and POLYMER, notwithstanding that our analysis allows a higher level of generality. Non-existence of vicarious gains, in the standard sense, is the primary feature of any spectral-matching algorithm and justifies extending SVC in a least-square sense. Multiplicity of POLYMER gains, i.e. the possibility of totally different gains to yield to very same marine reflectance, results at first sight from algorithmic specificities: the fact that POLYMER aerosol reflectance depends linearly on the three coefficients (c_0, c_1, c_2) and that inversion deals with the singular matrix M. In fact, even in the standard case, gains in the visible are unique only because the NIR vicarious calibration is preliminary fixed. It is well-known since Wang and Gordon (2002) that NIR gains are somewhat arbitrary (at least over a reasonable range of amplitude and for moderate aerosol content) thanks to gains in the visible compensating for any bias related to aerosol; this has been further verified in the operational SVC of NASA (Franz et al. 2007). Hence, multiplicity must rather be understood as an unavoidable issue due to the simultaneous gain computation at all bands. In the standard SVC it vanishes de facto by the two-step approach. For POLYMER, we have seen that fixing three gains in the NIR allows also fixing the three spectral coefficients.

Relevance of SVC is mentioned in Table 14 in reference to preceding section, that is to say for assessing how much SVC improves performance of the atmospheric correction (first on the calibration site, then more globally). Although the improvement may be only reached in a weak sense (trade-off between bands), this still implicitly assumes a strong link between the TOA calibration and the BOA retrieval, effectively observed for POLYMER. However, such direct relationship is not necessarily true for any non-standard atmospheric correction, which might limit once more the scope of SVC, as discussed hereafter.

Table 14. Summary of differences in SVC gains between standard (left) and spectral matching (right) atmospheric correction algorithm. Properties are stated for pixel-by-pixel (individual) gains except for last line relevant to the mission average gains.

	Standard atmospheric correction (Gordon & Wang)	Spectral matching (POLYMER)
Existence	Gains always exists	Strict gains only exist if marine model exactly fits in-situ data
Uniqueness	Gains are unique, relatively to a first NIR calibration	Multiplicity of gains are possible; need to fix some bands
Computation	Gains are computed explicitly at each band	Gains are computed numerically to solve a non-linear spectrally coupled system
Relevance	Gains yield a perfect match with reference data at all bands	Gains yield an approximate match, in a least-square sense; error vary with bands
Bias removal	Average gains remove bias by construction	Average gains do not strictly remove the bias due to non-linear effect

Our approach gives a new insight on vicarious calibration: solving Eq. (12) equivalent to finding out how much we have to change the TOA radiometry so that the processing (mainly atmospheric correction) yields the targeted BOA signal, at least in an optimal sense. Hence sensitivity of marine reflectance to TOA radiometry is the key factor to grasp the potential of a vicarious calibration. Schematically we can classify atmospheric correction algorithms in two families, having their own advantages and drawbacks:

- When atmospheric correction is linearly sensitive to radiometry (standard scheme case):
    - Marine reflectance depends strongly on instrumental calibration, which can yield to noise or bias in the data

    - But bias can always be corrected with vicarious gains (at least at pixel level)
- When atmospheric correction involves non-linearly all bands together:
    - Marine reflectance is probably more robust to instrumental calibration and noise
    - But it is more difficult to find vicarious gains – if feasible, which is not insured because of spectral coupling and possibly weak sensitivity of some bands

POLYMER is part of the second family, and despite its relatively complex link between TOA and BOA radiometry it presents enough sensitivity for benefiting from a SVC, as previously demonstrated. On the other hand, should an atmospheric correction scheme induce bias at some bands and be too insensitive then a vicarious calibration would be simply inoperative.

The relative importance of the marine model embedded in the atmospheric correction, versus TOA calibration, incites us to broaden our common view on SVC. In the standard case, the highest priority is set on the source of in-situ data used for calibration because SVC can always remove the global bias, whatever the errors of atmospheric correction at match-up level. For instance, Zibordi et al. (2015) derived requirements on in-situ data when considering the standard scheme and furthermore by assuming it retrieves perfectly the atmospheric path reflectance. These are two strong assumptions not satisfied in our present context. If such requirements are certainly necessary to build reference dataset of high accuracy, they are not sufficient to remove systematic error of POLYMER. In practice, the role of atmospheric correction is at least as much important as that of in-situ data used to compute gains. For POLYMER, we have checked that the overall performance is impacted more by the model parameterisation than by a TOA calibration of few percent (not shown here; see section 2 for a brief summary of two parameterisations). Hence improving modelling should be the first priority of spectral-matching atmospheric correction, keeping in mind that SVC cannot entirely remove systematic error.

6. References

Ahn, J., Park, Y., Kim, W., Lee, B. and Oh, I. (2015). Vicarious calibration of the Geostationary Ocean Color Imager. Opt. Express 23, 23236-23258.

Antoine D. and Morel A. (1999). A multiple scattering algorithm for atmospheric correction of remotely-sensed ocean colour (MERIS instrument): principle and implementation for atmospheres carrying various aerosols including absorbing ones. Int. J. Rem. Sens., 20(9): 1875-1916.

Antoine, D., Vellucci, V., Banks, A.C., Bardey, P., Bretagnon, M., Bruniquel, V., Deru, A., Fanton d'Andon, O.H., Lerebourg, C., Mangin, A., Crozel, D., Victori, S., Kalampokis, A., Karageorgis, A.P., Petihakis, G., Psarra, S., Golbol, M., Leymarie, E., Bialek, A., Fox, N., Hunt, S., Kuusk, J., Laizans, K., and Kanakidou, M. (2020). ROSACE: A proposed European Design for the Copernicus Ocean Colour System Vicarious Calibration Infrastructure. Remote Sensing 12, 1535. https://doi.org/10.3390/rs12101535.

Bailey, S. W., and Werdell, P.J. (2006). A multi-sensor approach for the on-orbit validation of ocean color satellite data products. Remote Sensing of Environment 102, 12-23.

Bailey, S.W., Hooker, S. B., Antoine, D., Franz, B. A., and Werdell, P. J. (2008). Sources and assumptions for the vicarious calibration of ocean color satellite observations. Applied Optics, 47, 2035–2045.

Bailey, S. W., Franz, B. A. and Werdell, P. J. (2010). Estimations of near-infrared water-leaving reflectance for satellite ocean color data processing. Opt. Express 18(7), 7521–7527.

Baith, K., Lindsay, R., Fu, G. and McClain, C. R. (2001). Data analysis system developed for ocean color satellite sensors. EOS. Trans. AGU 82, 202.

Barnard A., Boss E., Haëntjens N., Orrico C., Chamberlain P., Frouin R., Mazloff M. and Tan J. (2024) A float-based Ocean color vicarious calibration program. Front. Remote Sens. 5:1373540. doi: 10.3389/frsen.2024.1373540

Brewin, R. J. W., Mélin, F., Sathyendranath, S., Steinmetz, F., Chuprin, A., Grant, M. (2014). On the temporal consistency of chlorophyll products derived from three ocean-colour sensors. ISPRS Journal of Photogrammetry and Remote Sensing, 97, 171-184.

Bricaud, A., and Morel, A. (1987). Atmospheric corrections and interpretation of marine radiances in CZCS imagery: use of a reflectance model. Oceanologica Acta, N°SP, 33-50.

Brockmann, C., Ruescas, A., and Stelzer, K. (2011). OC-CCI Pixel Identification. ESA OC-CCI Algorithm Theoretical Basis Document ref. AO-1/6207/09/I-LG, Issue 1.

Brown, S.W., Flora, S.J., Feinholz, M.E., Yarbrough, M.A., Houlihan, T., Peters, D., Kim, Y. S., Mueller, J., Johnson, B.C., Clark, D.K. (2007). The Marine Optical BuoY (MOBY) radiometric calibration and uncertainty budget for ocean color satellite sensor vicarious calibration. Proc. SPIE Optics and Photonics; Sensors, Systems, and Next-Generation Satellites XI.

Chomko, R. M., Gordon, H. R., Maritonera, S., and Siegel, D. A. (2003). Simultaneous retrieval of oceanic and atmospheric parameters for ocean color imagery by spectral optimization: A validation. Remote Sensing of Environment, 84, 202−220.

Chamberlain, P., R. J. Frouin, J. Tan, M. Mazloff, A. Barnard, E. Boss, N. Haëntjens, and C. Orrico (2024). Selecting HyperNav deployment sites for calibrating and validating PACE ocean color observations. Front. Remote Sens., 5, 1333851, https://doi.org/10.3389/frsen.2024.1333851.

Clark, D. K., H. R. Gordon, K. J. Voss, Y. Ge, W. Broenkow, and C. Trees (1997). Validation of atmospheric correction over the oceans. J. Geophys. Res., 102, 17 209–17 217, https://doi.org/10.1029/96JD03345.

Clark, D.K., Yarbrough, M. A., Feinholz, M. E., Flora, S., Broenkow, W., Kim, Y. S., Johnson, B. C., Brown, S. W., Yuen, M., and Mueller, J. L. (2003). MOBY, a radiometric buoy for performance monitoring and vicarious calibration of satellite ocean color sensors: Measurement and data analysis protocols, in Ocean Optics Protocols for Satellite Ocean Color Sensor Validation, Revision 4, Volume VI: Special Topics in Ocean Optics Protocols and Appendices. NASA/TM-2003-211621/Rev4-Vol.VI:3-34, Greenbelt, MD.

Cox, C., and Munk, W. (1954). Measurement of the roughness of the sea surface from photographs of the sun's glitter. J. Opt. Soc. Am. 44(11), 838-850.

Delwart, S. and Bourg, L. (2013). MERIS calibrations: 10 years. Proc. SPIE 8866, Earth Observing Systems XVIII, 88660Y (September 23, 2013).

Doerffer, R. and Schiller, H. (2007). The MERIS Case 2 water algorithm. International Journal of Remote Sensing, 28, 517–535.

Doerffer, R. (2015). Level-2 processing of MERIS data of case 2 waters, ATBD of MERIS 4th reprocessing, issue no 2.

Eplee, R. E., Robinson, W. D., Bailey, S. W., Clark, D. K., Werdell, P. J., Wang, M., Barnes, R. A., McClain, C. R. (2001). Calibration of SeaWiFS. II. Vicarious techniques. Applied Optics, 40, 6701–6718.

Eplee, R. E., Jr., Sun, J. -Q., Meister, G., Patt, F. S., Xiong, X., & McClain, C. R. (2011). Cross calibration of SeaWiFS and MODIS using on-orbit observations of the moon. Applied Optics, 50, 120–133.

EUMETSAT (2017). Requirements for Copernicus Ocean colour vicarious calibration infrastructure. Reference SOLVO/EUM/16/VCA/D8, 92 pp., https://ioccg.org/wp-content/uploads/2018/04/cop_ocean_col_cal.pdf.

Evans, R. H., and Gordon, H. R. (1994). CZCS 'System Calibration': a retrospective examination. Geophys. Res. 99C: 7293-7307.

Fan, Y., W., Li, N., Chen, J.-H., Ahn, Y.-J., Park, S., Kratzer, T., Schroeder, J., Ishizaka, R., Chang and K., Stamnes (2021). OC-SMART: A machine learning based data analysis platform for satellite ocean color sensors, Remote Sensing of Environment, 253, https://doi.org/10.1016/j.rse.2020.112236.

Feng, H., Vandemark, D., Campbell, J. W., and Holben, B. N. (2008). Evaluation of MODIS ocean color products at a northeast United States coast site near the Martha's Vineyard Coastal Observatory. International Journal of Remote Sensing, 29, 4479−4497.

Franz, B. A., Bailey, S. W., Werdell, P. J., & McClain, C. R. (2007). Sensor-independent approach to the vicarious calibration of satellite ocean color radiometry. Applied Optics, 46, 5068–5082.

Frouin, R. and Pelletier, B (2015). Bayesian methodology for inverting satellite ocean-color data. Remote Sensing of Environment, 159: 332 –360.

Frouin, R., Tan, J., Barnard, A., Bailess, A., Boss, E., Haëntjens, N., Banks, A., Chamberlain, P., and Mazloff, M. (2025). System Vicarious Calibration of the PACE Ocean Color Instrument, EGU General Assembly 2025, Vienna, Austria, 27 Apr–2 May 2025, EGU25-20694, https://doi.org/10.5194/egusphere-egu25-20694.

Gordon, H. R. (1978). Removal of atmospheric effects from satellite imagery of the oceans. Appl. Opt. 17, 1631 –1636.

Gordon, H. R. (1987). Calibration requirements and methodology for remote sensors viewing the ocean in the visible. Remote Sensing of Environment, 22, 103–126.

Gordon, H. R. (1998). In-orbit calibration strategy for ocean color sensors. Remote Sensing of Environment, 63, 265-278.

Gordon, H. R. and Wang, M. (1994). Retrieval of water-leaving radiance and aerosol optical thickness over the oceans with SeaWiFS: A preliminary algorithm. Appl. Optics, 33: 443-452.

Hollmann, R., Merchant, C. J., Saunders, R., Downy, C., Buchwitz, M., Cazenave, A., Chuvieco, E., Defourny, P., De Leeuw, G., Forsberg, R., Holzer-Popp, T., Paul, F., Sandven, S., Sathyendranath, S., van Roozendael, M., Wagner, W. (2013). The ESA Climate Change Initiative: satellite data records for essential climate variables. Bulletin of the American Meteorological Society, 94 (10), pp.1541-1552.

Hu, C., Feng, L., Lee, Z-P., Davis, C.O., Mannino, A., McClain, C.R., and Franz, B.A. (2012). Dynamic range and sensitivity requirements of satellite ocean color sensors: learning from the past. Applied Optics, 51(25): 6045-6062.

IOCCG (2025). Evaluation of Atmospheric Correction Algorithms over Turbid Waters. Jamet, C., Balasubramanian, S. V. (eds.), IOCCG Report Series, No. 21, International Ocean Colour Coordinating Group, Dartmouth, Canada.

Kuchinke, C. P., Gordon, H. R., and Franz, B. A. (2009). Spectral optimization for constituent retrieval in Case II waters I: Implementation and performance. Remote Sensing of Environment, 13, 571−587.

Lebreton, C., Stelzer, K., Brockmann, C., Bertels, L., Pringle, N., Paperin, M., Danne, O., Knaeps, E., and Ruddick, K. (2016). Cloud and cloud shadow masking of high and medium resolution optical sensors - an algorithm inter-comparison example for Landsat-8. Proceedings of the 2016 ESA Living Planet Symposium held in Prague, Czech Republic, 9-13 May 2016, ESA Special Publication SP-740.

Lerebourg, C., Mazeran, C., Huot, J., & Antoine, D. (2011). Vicarious adjustment of the MERIS ocean colour radiometry. MERIS ATBD 2.24 issue 1.0.

Liberti, G.L., D'Alimonte, D., di Sarra, A., Mazeran, C., Voss, K., Yarbrough, M., Bozzano, R., Cavaleri, L., Colella, S., Cesarini, C., Kajiyama, T., Meloni, D., Pomaro, A., Volpe, G., Yang, C., Zagolski, F., Santoleri, R., (2020). European Radiometry Buoy and Infrastructure (EURYBIA): A Contribution to the Design of the European Copernicus Infrastructure for Ocean Colour System Vicarious Calibration. Remote Sensing 12(7), 1178. https://doi.org/10.3390/rs12071178.

Maritorena S., O. Hembise Fanton d'Andon, A. Mangin, and D.A. Siegel. (2010). Merged Satellite Ocean Color Data Products Using a Bio-Optical Model: Characteristics, Benefits and Issues. Remote Sensing of Environment, 114, 8: 1791-1804.

Mazeran, C., and Ruescas, A. (2020). Ocean Colour System Vicarious Calibration Tool. Tool documentation ref. EUM/19/SVCT/D2, issue 1.0.

Mélin, F., G. Zibordi, and S. Djavidnia (2009). Merged series of normalized water leaving radiances obtained from multiple satellite missions for the Mediterranean Sea. Adv. Space Res. 43, 423 –437.

Mélin, F. and Giuseppe Zibordi (2010). Vicarious calibration of satellite ocean color sensors at two coastal sites. Applied Optics, 49, 798-810.

Morel, A., and Gentili, B. (1996). Diffuse reflectance of oceanic waters. 3. Implication of bidirectionality for the remote-sensing problem. Applied Optics, 35, 4850-4862.

Morel, A., and Maritorena, S. (2001). Bio-optical properties of oceanic waters: A reappraisal. Journal of Geophysical research, 106, 7763-7780.

Morel, A., Antoine, D. and Gentili, B. (2002). Bidirectional reflectance of oceanic waters: Accounting for Raman emission and varying particle phase function, Applied Optics, 41, 6289-6306.

Mueller, L., Clark, D. K., Kuwahara, V. S., Lazin, G., Brown, S., Fargion, G. S., Yarbrough, M. A., Feinholz, M., Flora, S., Broenkow, W., Kim, Y. S., Johnson, B. C., Yuen, M., Strutton, P. G., Dickey, T. D., Abbott, M. R., Letelier, R. M., Lewis, M. R., McLean, S., Chavez, F. P., Barnard, J. R. M. A., Subramaniam, A., Manov, D., Zheng, X., Harding, J. L. W., Barnes, R. A., and Lykke, K. R. (2003). Ocean optics protocols for satellite ocean color sensor validation, Revision 4, Volume VI: Special topics in ocean optics protocols and appendices. NASA/TM-2003-211621/Rev4-Vol.VI, Greenbelt, MD.

Müller, D., Krasemann, H., Brewin, R. J. W., Brockmann, C., Deschamps, P.-Y., Doerffer, R., Fomferra, N., Franz, B. A., Grant, M. G., Groom, S. B., Mélin, F., Platt, T., Regner, P., Sathyendranath, S., Steinmetz, F., Swinton J. (2015). The Ocean Colour Climate Change Initiative: II. A methodology for assessing atmospheric correction processors based on in-situ measurements. Remote Sensing of Environment, 162, 242-256.

O'Kane, S., McCarthy, T., Fealy, R., & Kratzer, S. (2024). A Validation of OLCI Sentinel-3 Water Products in the Baltic Sea and an Evaluation of the Effect of System Vicarious Calibration (SVC) on the Level-2 Water Products. Remote Sensing, 16(21), 3932. https://doi.org/10.3390/rs16213932.

Park, Y., and Ruddick, K. (2005). Model of remote-sensing reflectance including bidirectional effects for case 1 and case 2 waters. Applied Optics 44:1236–1249.

Patt, F. S., Barnes, R. A., Eplee R. E., Franz, B. A., Robinson, W. D., Feldman, G. C., Bailey, S. W., Gales, J., Werdell, P. J., Wang, M., Frouin, R., Stumpf, R. P., Arnone, R. A., Gould, J. R. W., Martinolich, P. M., Ransibrahmanakul, V., O'Reilly, J. E., and Yoder, J. A. (2003). Algorithm updates for the Fourth SeaWiFS data reprocessing. NASA/TM-2003-206892, Vol. 22, Greenbelt, MD.

Ruddick, K., De Cauwer, V., Park, Y. and Moore, G. (2006). Seaborne measurements of near infrared water-leaving reflectance: The similarity spectrum for turbid waters. Limnology and Oceanography, Vol. 51(2) pp. 1167–1179.

Sathyendranath, S., Brewin, R. J. W., Brockmann, C., Brotas, V., Calton, B., Chuprin, A., Cipollini, P., Couto, A. B., Dingle, J., Doerffer, R., Donlon, C., Dowell, M., Farman, A., Grant, M., Groom, S., Horseman, A., Jackson, T., Krasemann, H., Lavender, S., Martinez-Vicente, V., Mazeran, C., Mélin, F., Moore, T., Müller, D., Regner, P., Roy, S., Steel, C., Steinmetz, F., Swinton, J., Taberner, M., Thompson, A., Valente, A., Zühlke, M., Brando, V., Feng, H., Feldman, G., Franz, B., Frouin, R., Gould Jr, R., Hooker, S., Kahru, M., Kratzer, S., Mitchell, G., Muller-Karger, F., Sosik, H., Voss, K., Werdell, J., Platt, T. (2019). An Ocean-Colour Time Series for Use in Climate Studies: The Experience of the Ocean-Colour Climate Change Initiative (OC-CCI). Sensors, 19(19), 4285. https://doi.org/10.3390/s19194285.

Schroeder, T., Behnert, I., Schaale, M., Fischer, J., and Doerffer, R. (2007). Atmospheric correction algorithm for MERIS above case-2 waters. International Journal of Remote Sensing, 28, 1469–1486.

Siegel, D. A., M. Wang, S. Maritorena, and, W. Robinson (2000). Atmospheric correction of satellite ocean color imagery: The black pixel assumption. Appl. Opt. 39(21), 3582–3591.

Spurr, R., K. Stamnes, H. Eide, W. Li, K. Zhang, and J. Stamnes. (2007). Simultaneous retrieval of aerosol and ocean color: A classic inverse modeling approach: I. Analytic Jacobians from the linearized CAO-DISORT model. J. Quant. Spectrosc. Radiative Transfer. 104, 428-449.

Steinmetz, F., Deschamps, P.-Y., and Ramon, D. (2011). Atmospheric correction in presence of sun glint: application to MERIS. Optics Express, Vol. 19, Issue 10: 9783-9800.

Steinmetz F., Ramon, D., Deschamps, P. Y. (2015). POLYMER atmospheric correction algorithm. ESA OC-CCI Algorithm Theoretical Basis Document, Issue 2.0.

Steinmetz, F., and Mazeran, C. (2021). SACSO: Atmospheric Aerosol Correction for Sentinel-3 Ocean Colour. EUMETSAT ATBD ref EUM/19/SACSO/ATBD, version 2.1. Available at https://www.eumetsat.int/media/48873

Wang, M., and Gordon, H.R. (2002). Calibration of ocean color scanners: how much error is acceptabel in the near infrared? Remote Sensing of Environment, 82: 497-504.

Wang, M., Shi, W., Jiang, L., Voss K. (2016). NIR- and SWIR-based on-orbit vicarious calibrations for satellite ocean color sensors. Optics Express 24(18): 20437-20453.

Wang, J., Chen, S., Hu, S., Deng, L., Ma, C., Peng, H., Song, Q. (2025). System vicarious calibration and ocean color retrieval from the HY-1C UVI. International Journal of Applied Earth Observation and Geoinformation, Volume 136, 2025, 104417, ISSN 1569-8432, https://doi.org/10.1016/j.jag.2025.104417.

Wang, M. and L. Jiang (2025). On-orbit system vicarious calibrations for three VIIRS sensors using the NIR-SWIR ocean color data processing approach. IEEE Trans. Geosci. Remote Sens., 63, 4203416, 2025. https://doi.org/10.1109/tgrs.2025.3542331

Werdell, P. J. and Bailey, S. W. (2005). An improved in-situ bio-optical data set for ocean color algorithm development and satellite data product validation. Remote Sens. Environ. 98, 122–140.

World Meteorological Organization (WMO) (2010). Implementation plan for the global observing system for climate in support of the UNFCCC (2010 update). GCOS report 138.

World Meteorological Organization (WMO) (2011). Systematic observation requirements for satellite-based data products for climate (2011 update). GCOS report 154.

World Meteorological Organization (WMO) (2022). The 2022 GCOS ECV requirements. GCOS report 245.

245.

Zibordi, G., Berthon, J.-F., Bulgarelli, B., D'Alimonte, D., van der Linde, D. , Mélin, F., and Targa, C. (2004). Ocean color validation activities at the Acqua Alta Oceanographic Tower in the Northern Adriatic Sea. International Journal of Remote Sensing, 25, 1533–153.

Zibordi, G., Holben, B., Hooker, S. B., Mélin, F., Berthon, J. -F., Slutsker, I., Giles, I., Vandemark, D., Feng, H., Rutledge, K., Schuster, G., and Al Mandoos, A. (2006a). A network for standardized ocean color validation measurements. EOS Trans. AGU, 87(293), 297.

Zibordi, G., Strömbeck, N., Mélin, F., and Berthon, J.-F. (2006b). Tower based radiometric observations at a coastal site in the Baltic Proper. Estuar. Coast. Shelf Sci. 69, 649–654.

Zibordi, G., Berthon, J. F., Mélin, F., D'Alimonte, D. and Kaitala, S. (2009a). Validation of satellite ocean color primary products at optically complex coastal sites: Northern Adriatic Sea, northern Baltic Proper and Gulf of Finland. Remote Sens. Environ. 113: 2574-2591.

Zibordi, G., Holben, B. N., Slutsker, I., Giles, D., D'Alimonte, D. , Mélin, F., Berthon, J.-F., Vandemark, D., Feng, H., Schuster, G., Fabbri, B. E., Kaitala, S., and Seppäl, J. (2009b). AERONET-OC: a network for the validation of ocean color primary radiometric products. J. Atmos. Ocean. Technol. 26, 1634–1651.

Zibordi, G., Melin, F., Voss, K., Johnson, B., Franz, B., Kwiatkowska, E., Huot J-P., Wang, M., and Antoine D. (2015). System vicarious calibration for ocean color climate change applications: Requirements for in situ data. Remote Sensing of Environment. 159 361-369.

Zibordi, G., and F. Mélin (2017). An evaluation of marine regions relevant for ocean color system vicarious calibration. Remote Sens. Environ., 190, 122–136, https://doi.org/10.1016/j.rse.2016.11.020.

Zibordi, G., Johnson, B. C., Kwiatkowska, E., Voss, K. J., Antoine, D., Barnard, A., Barnes, B. B., Mélin, F., Wang, M., Bialek, A., Bailey, S., & Chen, S. (2025). System Vicarious Calibration for Climate and Global Long-Term Operational Ocean Color Applications. Bulletin of the American Meteorological Society, 106(2), E394-E407. https://doi.org/10.1175/BAMS-D-24-0085.1